

# Gravitational Microlensing Events Due to Stellar Mass Black Holes<sup>1</sup>

D.P. Bennett<sup>2,3</sup>, A.C. Becker<sup>4</sup>, J.L. Quinn<sup>2</sup>, A.B. Tomaney<sup>5</sup>, C. Alcock<sup>3,6,7</sup>, R.A. Allsman<sup>8</sup>, D.R. Alves<sup>9</sup>,  
 T.S. Axelrod<sup>10</sup>, K.H. Cook<sup>3,7</sup>, A.J. Drake<sup>7</sup>, P.C. Fragile<sup>2</sup>, K.C. Freeman<sup>10</sup>, M. Geha<sup>11</sup>, K. Griest<sup>12</sup>,  
 B.R. Johnson<sup>13</sup>, S.C. Keller<sup>7</sup>, C. Laws<sup>5</sup>, M.J. Lehner<sup>6</sup>, S.L. Marshall<sup>7</sup>, D. Minniti<sup>14</sup>, C.A. Nelson<sup>7,15</sup>,  
 B.A. Peterson<sup>10</sup>, P. Popowski<sup>16</sup>, M.R. Pratt<sup>5</sup>, P.J. Quinn<sup>17</sup>, S.H. Rhee<sup>2</sup>, C.W. Stubbs<sup>3,5</sup>, W. Sutherland<sup>18</sup>,  
 T. Vandehei<sup>12</sup>, D. Welch<sup>19</sup>

(The MACHO and MPS Collaborations)

## ABSTRACT

We present an analysis of the longest timescale microlensing events discovered by the MACHO Collaboration during a seven year survey of the Galactic bulge. We find six events that exhibit very strong microlensing parallax signals due, in part to accurate photometric data from the GMAN and MPS collaborations. The microlensing parallax fit parameters are used in a likelihood analysis, which is able to estimate the distance and masses of the lens objects based upon a standard model of the Galactic velocity distribution. This analysis indicates that the most likely masses of five of the six lenses are  $> 1 M_{\odot}$  which suggests that a substantial fraction of the Galactic lenses are massive stellar remnants. The lenses for events MACHO-96-BLG-5 and MACHO-98-BLG-6 are the most massive, with mass estimates of  $M/M_{\odot} = 6^{+10}_{-3}$  and  $M/M_{\odot} = 6^{+7}_{-3}$ , respectively. The observed upper limits on the absolute brightness of these lenses are  $\lesssim 1 L_{\odot}$ , so both lenses are black hole candidates. We consider the possibility that the source stars for some of these six events may lie in the foreground Galactic disk or in the Sagittarius (SGR) Dwarf Galaxy behind the bulge, but we find that bulge sources are likely to

<sup>1</sup>Based in part on Observations from NASA's Hubble Space Telescope

<sup>2</sup>Department of Physics, University of Notre Dame, IN 46556

<sup>3</sup>Center for Particle Astrophysics, University of California, Berkeley, CA 94720

<sup>4</sup>Bell Laboratories, Lucent Technologies, 600 Mountain Avenue, Murray Hill, NJ 07974

<sup>5</sup>Departments of Astronomy and Physics, University of Washington, Seattle, WA 98195

<sup>6</sup>Department of Physics and Astronomy, University of Pennsylvania, Philadelphia, PA, 19104-6396

<sup>7</sup>Lawrence Livermore National Laboratory, Livermore, CA 94550

<sup>8</sup>Supercomputing Facility, Australian National University, Canberra, ACT 0200, Australia

<sup>9</sup>Space Telescope Science Institute, 3700 San Martin Dr., Baltimore, MD 21218

<sup>10</sup>Research School of Astronomy and Astrophysics, Mount Stromlo Observatory, Cotter Road, Weston, ACT 2611, Australia

<sup>11</sup>Department of Astronomy and Astrophysics, University of California, Santa Cruz 95064

<sup>12</sup>Department of Physics, University of California, San Diego, CA 92039

<sup>13</sup>Tate Laboratory of Physics, University of Minnesota, Minneapolis, MN 55455

<sup>14</sup>Dept. de Astronomia, P. Universidad Catolica, Casilla 104, Santiago 22, Chile

<sup>15</sup>Department of Physics, University of California, Berkeley, CA 94720

<sup>16</sup>Max-Planck-Institut für Astrophysik, Karl-Schwarzschild-Str. 1, 85741 Garching bei München, Germany

<sup>17</sup>European Southern Observatory, Karl Schwarzschild Str. 2, D-85748 Garching bei München, Germany

<sup>18</sup>Department of Physics, University of Oxford, Oxford OX1 3RH, U.K.

<sup>19</sup>Department of Physics and Astronomy, McMaster University, Hamilton, Ontario, Canada, L8S 4M1

dominate our microlensing parallax event sample. Future HST observations of these events can either confirm the black hole lens hypothesis or detect the lens stars and provide a direct measurement of their masses. Future observations of similar events by SIM or the Keck or VLTI interferometers (Delplancke, Górska & Richichi 2001) will allow direct measurements of the lens masses for stellar remnant lenses as well.

## 1. Introduction

The abundance of old stellar remnants in our Galaxy is largely unknown because they emit little radiation unless they happen to be accreting material from a companion star, or for neutron stars, if they happen to emit pulsar radiation in our direction. Gravitational microlensing surveys (Liebes 1964; Paczyński 1986; Alcock et al. 1993; Aubourg et al. 1993; Udalski et al. 1993; Bond et al. 2001) have the potential to detect completely dark stellar remnants, but for most microlensing events, the mass can only be estimated very crudely based upon the observed Einstein ring diameter crossing time,  $\hat{t}$ . For an individual microlensing event, the mass can only be estimated so crudely that a  $7M_{\odot}$  black hole cannot be distinguished from a  $0.5M_{\odot}$  star. However, for some microlensing events, it is possible to measure other parameters besides  $\hat{t}$  that allow tighter constraints on the lens mass (Refsdal 1966; Gould 1992; Nemiroff & Wickramasinghe 1994; Alcock et al. 1995; Bennett et al. 1996; Han & Gould 1997; Alcock et al. 1997c; Afonso et al. 2000; Alcock et al. 2001a). For long timescale microlensing events, which are often due to massive lenses, it is frequently possible to measure the microlensing parallax effect (Refsdal 1966; Gould 1992; Alcock et al. 1995) which is an observable deviation in the microlensing light curve due to the orbital motion of the Earth. In this paper, we present an analysis of the microlensing events discovered by the MACHO Project which give a very strong microlensing parallax signal, and we show that some of these events are best explained as microlensing by black holes.

This paper is organized as follows: in Sections 2 and 3, we discuss the microlensing event data set and the long timescale sub-sample. The microlensing parallax fits are presented in Section 4, and in Section 5 we present our main analysis to determine the distances and masses of the lenses. This includes a discussion of the projected lens velocity distributions, the source star color magnitude diagrams, and a likelihood analysis of the distances and masses of the microlenses. In Section 6, we discuss possible follow-up observations with high resolution telescopes and interferometers that can directly determine the microlensing parallax event lens masses, and we conclude in Section 7.

## 2. The Data Set

The MACHO Project (Alcock et al. 1993) has monitored  $\sim 10 - 20$  million stars in the Galactic bulge for 6-7 months per year during each of the 1993-1999 Galactic bulge seasons. During the last half of 1994, real-time microlensing discovery with the MACHO Alert system became possible (Alcock et al. 1996). (The OGLE collaboration developed this capability the same year (Udalski et al. 1994b).) This

development allowed much more accurate photometry of the microlensing events, which were discovered in progress, from the CTIO 0.9m telescope where the MACHO/GMAN Project was allocated about 1 hour every night (Becker 2000). In 1997, the Microlensing Planet Search (MPS) Project (Rhie et al. 1999) began microlensing follow-up observations from the Mt. Stromlo 1.9m telescope.

The data set used for this analysis consists of the MACHO survey data from the Mt. Stromlo 1.3m “Great Melbourne” telescope for all seven years, CTIO 0.9m data of selected alert events from 1995-1999, and Mt. Stromlo 1.9m data of alert events from the MPS 1997-1999 data sets. The initial selection of events consists of 42 events from 1993 (Alcock et al. 1997b), 252 events discovered by the MACHO Alert system from 1995-1999 (available from <http://darkstar.astro.washington.edu/>), and an additional 27 events discovered during the testing of the alert system, for a grand total of 321 events. There are  $\sim 200$  additional Galactic bulge events that have been discovered via other analyses that we have not considered here. A microlensing parallax study of a larger number of MACHO Alert events is presented in Becker (2000).

The MACHO and MPS data were reduced with slightly different versions of the SoDOPHOT photometry code (Bennett et al. 1993; Alcock et al. 1999). SoDOPHOT is quite similar to the DOPHOT photometry code (Schechter, Mateo, & Saha 1993) that it was derived from, but SoDOPHOT photometry generally exhibits smaller photometric scatter than DOPHOT photometry. This is due, in part, to SoDOPHOT’s error flags which allow the removal of suspect data points (Alcock et al. 1999), but the scatter in DOPHOT photometry is often increased by the user’s choice of PSF fitting parameters. Contrary to expectations, allowing the PSF fit box size to scale with the seeing generally causes increased photometric scatter (Bennett et al. 1993). The photometric errors reported by SoDOPHOT are modified by adding of 1.4% and 1.0% in quadrature to the MACHO and MPS data, respectively, to account for normalization and flat fielding errors. The CTIO data were reduced with the ALLFRAME package (Stetson 1994), with the error estimates multiplied by a factor of 1.5 to account for systematic errors.

### 3. Long Timescale Events

The timescale of a gravitational microlensing event is described by the Einstein diameter crossing time,  $\hat{t}$ , which depends on the lens mass ( $M$ ), distance ( $D_\ell$ ), and transverse velocity ( $v_\perp$ ). It is given by

$$\hat{t} = \frac{2R_E}{v_\perp} = \frac{4}{v_\perp c} \sqrt{\frac{GMD_\ell(D_s - D_\ell)}{D_s}}, \quad (1)$$

where  $D_s$  refers to the distance to the source (typically 8 kpc for a bulge source), and  $R_E$  is the radius of the Einstein Ring. Eq. (1) indicates that long  $\hat{t}$  events can be caused by large  $M$ , small  $v_\perp$  or both. Fig. 1 shows the long timescale tail of the  $\hat{t}$  distribution for our sample of 321 Galactic bulge microlensing events. In their analysis of the timescale distribution of the 1993 MACHO and OGLE bulge data sets, Han & Gould (1996) noted a surprisingly large fraction of the events with  $\hat{t} \geq 140$  days: 4/51 or 8%. Such a large fraction of long timescale events would be expected less than 2% of the time with any of the stellar mass functions that they considered. With our data set of 321 events, we find 28, or 9%, with  $\hat{t} > 140$  days.

The MACHO alert system is likely to be somewhat less sensitive to long timescale events than the 1993 analysis because the alert trigger is based upon the single most significant observation, so we would expect a slightly smaller fraction of long timescale events, but the fraction reported here is somewhat higher. The formal Poisson probability of 28/321 long events when 2% or less are expected is  $< 10^{-10}$ , so the excess of long timescale events over the Han & Gould (1996) models is highly significant. This disagreement may be due to a population of massive stellar remnants, including black holes, that was not included in the Han & Gould (1996) models, but there are other possibilities as well. Other explanations include a set of source-lens systems that have a low relative velocity from our vantage point in the Galactic disk or a more distant population of source stars.

The microlensing parallax effect refers to the effect of the orbital motion of the Earth on the observed microlensing light curve. The photometric variation for most microlensing events lasts only a month or two. For these events, the change in the Earth's velocity vector during the event is too small to generate a detectable deviation from the symmetric light curve, which is predicted for a constant velocity between the lens and the Earth-source star line of sight. For long timescale events, however, it is possible to see the effect of the Earth's motion in the microlensing light curve, and this is called the microlensing parallax effect.

#### 4. Microlensing Parallax Fits

The magnification for a normal microlensing event with no detectable microlensing parallax is given by

$$A(t) = \frac{u^2 + 2}{u\sqrt{u^2 + 4}} ; \quad u(t) \equiv \sqrt{u_0^2 + [2(t - t_0)/\hat{t}]^2} , \quad (2)$$

where  $t_0$  is the time of closest approach between the angular positions of the source and lens, and  $u_0 = b/R_E$  where  $b$  is the distance of the closest approach of the lens to the observer-source line. Eq. (2) can be generalized to the microlensing parallax case (Alcock et al. 1995) by assuming the perspective of an observer located at the Sun. We can then replace the expression for  $u(t)$  with

$$\begin{aligned} u^2(t) = & \ u_0^2 + \omega^2(t - t_0)^2 + \alpha^2 \sin^2[\Omega(t - t_c)] \\ & + 2\alpha \sin[\Omega(t - t_c)] [\omega(t - t_0) \sin \theta + u_0 \cos \theta] \\ & + \alpha^2 \sin^2 \beta \cos^2[\Omega(t - t_c)] + 2\alpha \sin \beta \cos[\Omega(t - t_c)] [\omega(t - t_0) \cos \theta - u_0 \sin \theta] \end{aligned} \quad (3)$$

where  $\lambda$  and  $\beta$  are the ecliptic longitude and latitude, respectively,  $\theta$  is the angle between  $v_{\perp}$  and the North ecliptic axis,  $\omega = 2/\hat{t}$ , and  $t_c$  is the time when the Earth is closest to the Sun-source line. The parameters  $\alpha$  and  $\Omega$  are given by

$$\alpha = \frac{\omega(1\text{AU})}{\tilde{v}} (1 - \epsilon \cos[\Omega_0(t - t_p)]) , \quad (4)$$

and

$$\Omega(t - t_c) = \Omega_0(t - t_c) + 2\epsilon \sin[\Omega_0(t - t_p)] , \quad (5)$$

where  $t_p$  is the time of perihelion,  $\Omega_0 = 2\pi \text{ yr}^{-1}$ ,  $\epsilon = 0.017$  is the Earth’s orbital eccentricity, and  $\tilde{v}$  is the lens star’s transverse speed projected to the Solar position, given by

$$\tilde{v} = v_{\perp} D_s / (D_s - D_{\ell}) , \quad (6)$$

The 28 events shown in Fig. 1 have been fit with the microlensing parallax model described by eqs. (2)-(4) which has 5 independent parameters:  $t_0$ ,  $u_0$ ,  $\hat{t}$ ,  $\tilde{v}$ , and  $\theta$ . In the crowded fields that are searched for microlensing, it is also necessary to include two parameters for each independent photometric pass band (or telescope) to describe the flux of the source star and the total flux of any unlensed stars that are not resolved from the lensed source. Thus, a microlensing parallax fit to the dual-color MACHO data alone will have 9 fit parameters, and a fit that includes the CTIO and MPS follow-up data will have 13 fit parameters.

The microlensing parallax fits were performed with the MINUIT routine from the CERN Library, and the results for the 6 events that we discuss in this paper are summarized in Table 2. The best fit light curves and data are shown in Figs. 2-7. The significance of the microlensing parallax signal is represented by the parameter  $\Delta\chi^2$  shown in Table 2 which is the difference between the fit  $\chi^2$  for a standard microlensing fit with no parallax (*i.e.*  $\tilde{v} = \infty$ ) and the best fit presented here. All 28 events with standard microlensing fits (including blending) which indicated  $\hat{t}_{\text{std}} > 140$  days were fit with a microlensing parallax model as well, and the 10 events with a microlensing parallax detection with a significance of  $\Delta\chi^2 \geq 50$  are indicated with color in Fig. 1. The four events with  $50 \leq \Delta\chi^2 < 200$  are MACHO-101-B, MACHO-95-BLG-27, MACHO-98-BLG-1, and MACHO-99-BLG-22, and the six strongest events with  $\Delta\chi^2 \geq 200$  are MACHO-104-C, MACHO-96-BLG-5, MACHO-96-BLG-12, MACHO-98-BLG-6, MACHO-99-BLG-1, and MACHO-99-BLG-8. These 6 events are the primary focus of this paper, and their coordinates are given in Table 1.

Note that most of the events with  $\hat{t} > 200$  days and all the events with  $\hat{t} > 300$  days have a significant parallax signal. Microlensing parallax is more easily detected in such long events because the Earth’s velocity changes significantly during the event, and because long events are likely to have low  $v_{\perp}$  values. There are also a number of events with much shorter timescales that appear to have microlensing parallax signals significant at the  $\Delta\chi^2 \geq 50$  level, but many of these have rather implausible parameters. This is likely to be due to the fact that other effects besides microlensing parallax can perturb the microlensing light curves in ways that can mimic the parallax effect. Examples of this include binary microlensing (see the discussion of MACHO-98-BLG-14 in Alcock et al. 2000a), and the reverse of the parallax effect, the orbital motion of a binary source star (Derue et al. 1999; Alcock et al. 2001a; Griest & Hu 1993; Han & Gould 1997), sometimes called the “xallarap” effect. The xallarap effect can be particularly difficult to distinguish from microlensing parallax because a xallarap light curve can be identical to a parallax light curve if the period, inclination, eccentricity, and phase mimic that of the Earth. In practical terms, this is a difficulty only when the xallarap or parallax signal-to-noise is weak so that the fit parameters are poorly determined.

In order to avoid contamination of our microlensing parallax sample with non-parallax microlensing events, we have set a higher threshold for the events that we study in detail in this paper:  $\Delta\chi^2 \geq 200$ . The 6 events that pass this threshold are listed in Tables 1 and 2. One of these events, MACHO-104-C, was the first microlensing parallax event ever discovered (Alcock et al. 1995), and the other five events were

discovered by the MACHO Alert system. Because of this, they had the benefit of follow-up observations by the MACHO/GMAN Collaboration on the CTIO 0.9m telescope or by the MPS Collaboration on the Mt. Stromlo 1.9m telescope. Four of these five events would have passed the  $\Delta\chi^2 \geq 200$  cut without the follow-up data, but event MACHO-98-BLG-6 only passes the cut because of the MPS follow-up data. This is probably due to a CCD failure that prevented the imaging of this event in the MACHO-Red band during most of the 1998 bulge season.

#### 4.1. HST Observations of MACHO-96-BLG-5

Event MACHO-96-BLG-5 is both the longest event in our sample<sup>1</sup>, and the event with the faintest source star. In fact, the microlensing parallax fit does not constrain the source star brightness very well. This is due to the faintness of the source, and due to a potential systematic error. The MACHO camera had a CCD upgrade in early 1999 which put a new CCD in the location that views MACHO-96-BLG-5 in the MACHO-Red passband. The new CCD probably had the effect of shifting the effective bandpass to a slightly different central wavelength, and so a slight systematic shift in the photometry of all the stars might be expected to occur with this upgrade. Because the MACHO-96-BLG-5 source is strongly blended with unlensed neighbors, the effect of this slight shift on the microlensing fit parameters can be relatively large because the fitting routine tries to explain all flux variation as resulting from microlensing. The best fit, with this suspect data removed, indicates that only about  $12 \pm 3\%$  of the flux associated with the “star” seen in our ground-based images has been microlensed, which would imply that the remaining 88% of the flux must come from unlensed neighboring stars which are within  $\sim 1.5''$  of the lensed source. Fortunately, we have a set of images from the Hubble Space Telescope’s WFPC2 Camera that can be used to constrain the brightness of the source star more accurately than the fit does.

We had one orbit of HST data taken in the V and I (F555W & F814W) passbands of the WFPC2 Camera through Director’s Discretionary Proposal # 8490, and this can be used to identify the microlensed source star. The first step in this identification process is to determine the centroid of the star that was lensed. This can be accomplished by subtracting two images which have substantially different microlensing magnifications (Alcock et al. 2001b). Since it is only the lensed source star that will appear to vary in brightness, this procedure will yield a point source centered on the location of the lens and source. Of course, the subtraction procedure must take into account the differences in the observing conditions of the two frames, including differences in seeing, pointing, sky brightness and air mass. We have accomplished this with the use of the DIFIMPHOT package of Tomaney & Crotts (1996).

A set of 18 of our best CTIO images were selected to use for this source location task because the CTIO images generally have better seeing than the MACHO images, and because the highest magnification of the source was only observed from CTIO. These 18 images were combined to construct a master reference

---

<sup>1</sup>The analysis of the MACHO and MPS data for MACHO-99-BLG-22 gives a best fit  $\hat{t} = 700$  days, but a combined analysis with the OGLE data yields a fit that is similar to the OGLE result (Mao et al. 2001) and gives  $\hat{t} = 1100$  days. This is about 10% longer than our result for MACHO-96-BLG-5.

image which was then subtracted from each individual frame to construct a set of 18 difference images. The difference frames which had a negative flux at the location of our target were inverted, and then all the difference images were combined to make the master difference image shown in Figure 8. The centroid of the excess flux in this master difference image can be determined to better than 0.01”.

In order to identify the lensed source star on the HST images, we must find the correct coordinate transformation to match the ground and HST frames, but this is complicated by the fact that most of the “stars” in the ground-based images actually consist of flux from several different stars that are blended together in the ground-based frames. We have dealt with this in two different ways: first, we used the HST images to select a list of stars that were much brighter than their near neighbors, so that their positions should not be greatly affected by blending in the ground-based images. Then, we convolved the HST data with a 1.2” FWHM Gaussian PSF to simulate the resolution of the ground-based CTIO data. We then analyzed the convolved HST image with the same data reduction software used for the ground-based data. This gave an additional star list from the HST image. Two independent coordinate transformations between the ground-based and HST data were obtained by matching these two stars list to the star list for the ground-based data.

The HST images were dithered, and we combined them with the Drizzle routine (Fruchter & Hook 1997) prior to the comparison with the ground-based data. The CTIO R-band data were compared to the HST I and V band images as well as sum of the I and V band images. Coordinate transformation were determined to match the CTIO image coordinates to each of these HST images using the bright, isolated stars in the HST images and with the HST images convolved to ground-based seeing. This resulted in a total of 6 different comparisons between the location of the lensed star in the CTIO image and the HST images. All these comparisons yielded the same lens star location on the HST frames to better than 0.02”, and this location coincides with the centroid of the star indicated in Fig. 8. This star was examined carefully in both the V and I images to determine if it could be a blend of more than one star. Model and DAOPHOT generated PSFs were subtracted at the centroid location of the lensed source, but no hint of any additional star was found. This star is very likely to be the source star for the MACHO-96-BLG-5 microlensing event.

The next step in the comparison of the HST and ground-based data is to determine what fraction of the flux of the object identified as a star in the ground-based frames is contributed by the source star identified in the HST images. This task is complicated by the fact that there is no close correspondence between the passbands of the ground based images and those used for the HST data. (This is due to the limitations imposed upon an HST Director’s Discretionary time proposal. We requested prompt images in V and I to confirm the photometric variation implied by the microlensing parallax model, but prompt imaging in R could not be justified. Imaging in R was obtained in a subsequent GO program, and the analysis of these data will appear in a future publication.) Presumably, some combination of the V and I band images would provide a good representation of the R band ground based image.

The determination of the lensed flux fraction was made as follows: Photometry of the V+I combined HST frame was obtained using the IRAF implementation of DAOPHOT (Stetson 1987) and also using SoDOPHOT. Both of these packages were also used to reduce the HST images which had been convolved

to mimic ground based seeing. The total stellar flux of isolated, bright stars was not conserved in these convolved images, so we found it necessary to renormalize the stellar flux in the convolved images to the ratio found for these isolated bright stars. This comparison yielded a flux fraction of 36% for the lensed component of the stellar blend identified as a single star in the ground-based images. We also followed this same procedure for the separate I and V images, and the results for the lensed flux fraction were quite similar as might be expected from the fit results shown in Table 2, which indicate no color dependence for the blending fit parameter. This is likely to be due to the fact that the stars contributing the blended light and the lensed source star are all main sequence stars of similar color which are just below the bulge turn-off.

We must also make a correction for the fact that the source star was still being magnified by the lens when the HST frames were taken. Because the event timescale depends upon the amount of blending that we determine from the HST analysis, it requires an iteration or two to find a fit that predicts the observed brightness of the lensed star in the HST frames. The best fit result is that the lensed source provides 33% of the total flux of the blended object that would be seen in the ground based frames in the absence of any microlensing magnification. At the time of the HST images, the lensing magnification was 1.063 according to this fit.

Finally, we should mention the possibility that the star identified with the lensed source centroid is not, in fact, a single star. The HST images reveal no evidence of a chance superposition of unrelated stars, so this is unlikely. However, it could be that the superposition is not due to chance. Suppose, for example, that the star we've identified as the MACHO-96-BLG-5 source is actually the superimposed images of the lens and source. While this is a logical possibility, we will show below that there is no plausible scenario for this to occur because the implied lens mass cannot be made compatible with the observed brightness of the lens plus source.

## 5. Lens Mass and Distance Estimates

The measurement of the projected speed of the lens,  $\tilde{v}$ , allows us to relate the lens mass to the lens and source distances

$$M = \frac{\tilde{v}^2 \hat{t}^2 c^2}{16G} \frac{D_s - D_\ell}{D_\ell D_s} = \frac{\tilde{v}^2 \hat{t}^2 c^2}{16G} \frac{1 - x}{x D_s}. \quad (7)$$

It is often assumed that the distance to the source,  $D_s$ , is already known, at least approximately, so this relation can be considered to give the lens mass as a function of distance. Given the lens distance, one can also work out the lens velocity with respect to the line-of-sight to the source,  $v_\perp$ . But, for some distances, the implied  $v_\perp$  value can be unreasonably small or large. Thus, with some knowledge of the Galactic velocity distribution, we can work out an estimate for the distance and mass of the lens. This has been done for the MACHO-104-C event using a likelihood method in Alcock et al. (1995). This analysis assumes that the source star resides in the Galactic bulge, which is true for the vast majority of microlensing events seen towards the Galactic bulge. The result of similar analyses for the events presented in this paper are summarized in Table 3 and in Figs. 11-13. However, the microlensing parallax events are selected from a sample of unusually long microlensing events, so it may be that their source star locations are atypical as

well. With the data currently available to us, we have two ways to investigate the location of the source stars for our microlensing parallax events. The first is to make use of the direction of projected velocity as determined by the microlensing parallax fit, and the second is to examine the location of the source star in a color-magnitude diagram of nearby stars. Another, perhaps more effective, discriminant between different source populations is radial velocity measurements. Radial velocities for some of the source stars have been measured by Cook et al. (2002), and they have provided us with some preliminary results.

### 5.1. Source Star Locations

The line-of-sight toward a Galactic bulge microlensing event passes through the Galactic disk, the bulge, and through the Sagittarius (SGR) Dwarf Galaxy behind the bulge. So, all of these are possible locations for the source stars. The variation in the source population/location can affect the inferred properties of the lens in several different ways:

1. **Microlensing rate:** The microlensing rate per source star is very much lower for foreground Galactic disk stars and very much higher for SGR Dwarf stars than for Galactic bulge stars. Thus, foreground disk stars and SGR Dwarf stars will be under-represented and over-represented, respectively, in samples of microlensed stars when compared to stars in the Galactic bulge.
2. **Microlensing parallax detectability:** some source star populations such as the foreground Galactic disk and the Sagittarius Dwarf Galaxy give rise to a larger fraction of events with microlensing parallax parameters that can be measured.
3. **Source distance:** A source at a greater distance than the nominal Galactic bulge distance will usually imply a lower lens mass since  $M$  is a decreasing function of  $D_s$  in eq. (7) (for fixed  $x$ ). Similarly, a smaller  $D_s$  implies a larger mass.
4. **Source velocity:** From eq. (6), we see that, for a fixed  $\tilde{v}$  value, a smaller  $v_{\perp}$  value implies a larger  $D_s$  which, in turn, implies a smaller lens mass. Smaller  $v_{\perp}$  values are expected for lensing of foreground disk sources since the source and lens would both share the Galactic rotation velocity of the Sun.

Several authors who have modeled microlensing parallax events (Mao 1999; Soszyński et al. 2001; Smith, Mao, & Woźniak 2001) have suggested that the source stars must be predominantly in the foreground Galactic disk because this makes a small  $v_{\perp}$  more likely. A disk source is the only possibility for the OGLE-1999-CAR-1 event since this star is located far from the bulge, but for events towards the Galactic bulge there are several factors that make a foreground disk source star less likely, including a much lower microlensing optical depth and a lower density of source stars. These are discussed in section 5.3, where we find that disk sources that are definitely in the foreground of the bulge at  $D_s \leq 5$  kpc are quite unlikely.

## 5.2. Projected Velocity Distributions

One distinguishing characteristic of microlensing parallax distributions for different source populations is the distribution of the projected velocity,  $\tilde{\mathbf{v}}$  including both the amplitude,  $\tilde{v}$ , and the direction  $\theta$ . We use a Galactic model in which the stars around us are moving with a velocity dispersion of about 30 km/sec in both directions normal to the line of sight to the bulge. The Sun rotates at a speed of +16 km/sec faster than the *kinematic* Local Standard of Rest (LSR) and is moving towards Galactic North at 7 km/sec (Dehnen & Binney 1998). The Galactic disk rotates with an approximately flat rotation curve at  $v \simeq 200$  km/sec, while the Galactic bulge probably has little rotation (Minniti 1996) and has a velocity dispersion of 80-100 km/sec (Spaenhauer, Jones, & Whitford 1992; Minniti 1996; Zoccali et al. 2001). The Sagittarius Dwarf Galaxy is moving at  $250 \pm 90$  km/sec in a direction that is only a few degrees away from Galactic North (Ibata et al. 1997).

The different velocity distributions of these source and lens populations lead to different expectations for the measured  $\tilde{\mathbf{v}}$  distributions for events from different source star populations. However, the observed  $\tilde{\mathbf{v}}$  distribution is strongly affected by selection effects since only a small fraction of microlensing events have detectable parallax signals. These selection effects can be difficult to precisely quantify because of the fact that much of the data taken for these events comes from follow-up programs with observing strategies that can be subjective and difficult to model. Therefore, instead of attempting a detailed simulation of the actual observing conditions, we investigate the  $\tilde{\mathbf{v}}$  distribution using a “toy model” of a microlensing survey and follow-up program. We assume a disk velocity dispersion of 30 km/s in each direction, with a flat rotation curve of 200 km/s and a bulge velocity dispersion of 80 km/s with no bulge rotation, and the density profiles are a standard double-exponential disk and a barred bulge as in Han & Gould (1996). We assume that events are observed for 7 months per year by a microlensing survey system that makes photometric observations with 5% accuracy every 3 days. Once an event is magnified by at least 0.5 magnitudes, daily follow-up observations start with an accuracy of 1% for each day. This simulated data are then fit with a standard, no-parallax microlensing model, and the  $\Delta\chi^2$  is determined. (Since we have not added noise to the light curves, the fit  $\chi^2 = 0$  when there is no microlensing parallax signal.) Events with  $\Delta\chi^2 \geq 200$  are considered microlensing parallax detections, and the  $\tilde{\mathbf{v}}$  values for these simulated detected events are shown in Figure 9. This figure uses Galactic coordinates in which the  $y$ -axis is the direction of Galactic disk rotation, and the  $z$ -axis is Galactic North.

A striking feature of Figure 9 is that all six of our strong microlensing parallax events have  $\tilde{\mathbf{v}}$  in the same quadrant with positive  $\tilde{v}_y$  and negative  $\tilde{v}_z$ . This is the region that is preferred for both bulge and SGR source stars, but not for foreground disk sources. In our simulations, 65% of the detectable SGR source events, and 50% of the detectable bulge sources, but only 29% of foreground disk sources lie in this quadrant.

One selection effect that affects each plot is that events with  $\tilde{\mathbf{v}}$  roughly parallel to the ecliptic plane are easier to detect than events where  $\tilde{\mathbf{v}}$  is approximately perpendicular to the ecliptic plane. This effect favors the positive  $\tilde{v}_y$ -negative  $\tilde{v}_z$  and negative  $\tilde{v}_y$ -positive  $\tilde{v}_z$  quadrants. The reason for this is that the Earth’s orbital motion only affects  $u(t)$  near peak magnification when  $\tilde{\mathbf{v}}$  is perpendicular to the ecliptic plane, but the orbital motion affects  $u(t)$  for a longer period of time when it is parallel to  $\tilde{\mathbf{v}}$ .

For the bulge sources, there is a preference for positive  $\tilde{v}_y$  motion because disk lens stars are passing inside of us at a higher angular velocity. If the source stars are rotating with us, as would be the case for disk sources in the foreground of the bulge, then the rotation is common to the source, lens and observer, and it has no effect. A smaller systematic effect occurs in the disk source case because the Sun is moving about 16 km/sec faster than the mean stellar motion around us. Thus, there is a slight enhancement of the abundance of negative  $\tilde{v}_y$  events.

For SGR source stars, signal of the SGR proper motion toward the Galactic North can clearly be seen in the strong concentration of events at negative  $\tilde{v}_z$  and positive  $\tilde{v}_y$ . (Since  $\tilde{v}$  is a lens–source velocity, the  $\tilde{v}$  signal is in the opposite direction of the SGR motion.) For bulge lenses, the 250 km/sec velocity is reduced to 90 km/sec by the projection effect, and for the disk lenses that make up the bulk of microlensing parallax sample for SGR sources, the typical  $\tilde{v}_z$  is  $-50$  km/sec or so. For SGR sources, and disk lenses, the combination of SGR proper motion and disk rotation put the majority of  $\tilde{v}$  values in the positive  $\tilde{v}_y$ -negative  $\tilde{v}_z$  quadrant where the alignment with the ecliptic plane makes the parallax effect easy to detect.

### 5.3. Microlensing Parallax Selection Effects

For comparison between the different source populations, it is necessary to consider several different selection effects. First, the microlensing rate for SGR sources behind our fields is a factor of  $\sim 6$  larger than for bulge source stars (Cseresnjes & Alard 2001), and the fraction of SGR events with detectable microlensing parallax signals is a factor of 3 larger for sources in SGR than for bulge sources. Thus, it would appear that the probability of detecting a microlensing parallax event for a SGR source is a factor of  $\sim 20$  higher than for a bulge source (assuming that the sources are bright enough for reasonably accurate photometry). Of course, Galactic bulge sources are much more numerous, so microlensing parallax events with Galactic bulge source stars are likely to be more numerous than events with SGR source stars by an amount that is difficult to estimate. We consider this in detail in Section 5.4 when we present the source star color-magnitude diagrams.

It is quite difficult to distinguish Galactic bulge stars from stars in the inner Galactic disk because they are at similar distances and their velocity distributions overlap. In fact, this distinction is likely to be somewhat artificial because the two components are likely to have merged due to their mutual gravitational interactions. Therefore, we will limit our consideration of foreground disk sources to stars with a distance  $< 5$  kpc. For stars at 5 kpc distance at a Galactic latitude of  $b = -3^\circ$ , the microlensing rate is a factor of about  $\sim 40$  lower than for Galactic bulge stars. (The optical depth is only a factor of  $\sim 20$  lower because of the longer time scales of disk-disk lensing events.) The physical density of disk stars is about an order of magnitude lower than the density of bulge stars, but there is also a volume factor that reduces the number of disk stars per unit distance modulus and solid angle by a factor of 4 at 5 kpc. The product of these factors yields a net suppression factor of 1/1600 for disk star lensing events for a fixed source star absolute magnitude.

This suppression factor must be multiplied by two enhancement factors. First, our simulations indicate

that the chances of detecting a microlensing parallax signal are about a factor of 5 larger for disk sources than for bulge source stars. This increases the suppression factor to  $\sim 1/320$ . There is an additional enhancement factor due to the fact that the foreground disk stars are intrinsically fainter and the stellar luminosity function rises for fainter stars, but the difference between the disk stars at 5 kpc and the bulge stars at 8 kpc is only 1 magnitude. From Holtzman et al. (1998) we see that this factor is at most  $\approx 10$  if we select a source magnitude such that is 1-2 magnitudes above the bulge main sequence turnoff. For magnitudes that correspond to bulge main sequence stars, it is less than a factor of two. Thus, we expect disk stars (with  $D < 5$  kpc) to contribute less than 1% of the total number of detectable microlensing parallax events, except for source stars that are 1-2 magnitudes above the bulge main sequence turn-off where they might account for as many as 3% of the microlensing parallax events with bulge source stars.

Inner disk stars at  $D > 5$  kpc will be accounted for by allowing their velocities to contribute to the assumed bulge velocity distribution. In fact, such inner disk stars are generally not excluded from star samples that are used to measure the bulge proper motion (Spaenhauer, Jones, & Whitford 1992; Zoccali et al. 2001). We will, therefore, classify all stars in the vicinity of the bulge ( $5 \text{ kpc} < D_s < 11 \text{ kpc}$ ) as bulge stars. Instead of trying to distinguish different, but overlapping, populations of source stars, we consider a single model including all these stars.

Stars on the far side of the disk have velocities that make it very unlikely to see the microlensing parallax effect, while foreground disk stars are unlikely to be microlensed at all. Therefore, the SGR dwarf provides the only “non-bulge” population of potential source stars that we will consider in the remainder of this paper.

#### 5.4. Color Magnitude Diagrams

Fig. 10 shows color-magnitude diagrams for all the stars within 2 arc minutes around each of our microlensing parallax source stars, with the lensed source indicated by a red circle. It is necessary to use different color magnitude diagrams for each event because of the large variation in reddening between different fields. By plotting only the stars within 2 arc minutes of our targets, we have minimized the variation in reddening.

These CM diagrams indicate that the MACHO-104-C and MACHO-96-BLG-12 source stars are located in the bulge red clump region, which means that they are likely to reside in the Galactic bulge. The MACHO-99-BLG-8 source star is more luminous than the red clump and is likely to be a bulge giant. Cook et al. (2002) find a radial velocity of  $v_r = 195 \pm 2 \text{ km/s}$  which confirms the bulge interpretation for this event. The MACHO-96-BLG-5 source star appears to be fainter than virtually all of the other stars in its CM diagram. This is a consequence of the extreme crowding of these Galactic bulge fields. The density of bright main sequence stars is  $\sim 2$  per square arc second, so main sequence stars are not individually resolved in these crowded Galactic fields. Instead, it is groups of unresolved main sequence stars that are identified as single stars, and it is these unresolved blends of multiple stars that make up the majority of the fainter objects identified as stars in these images. The majority of microlensed source stars in the Galactic bulge

are blended main sequence stars like the MACHO-96-BLG-5 source, but the microlensing parallax signal is easier to detect for brighter source stars.

The source stars for events MACHO-98-BLG-6 and MACHO-99-BLG-1 appear to be on the bulge sub-giant branch of the color magnitude diagram. They have a similar color to bulge red clump stars, but they are about 2 magnitudes fainter. This suggests that they could be red clump stars  $\sim 14$  kpc behind the bulge in Sagittarius (SGR) Dwarf Galaxy. This is about the only location on the color magnitude diagram where we might expect to see microlensing of SGR source stars, because SGR red clump stars are probably the only abundant type of SGR stars that are brighter than the bulge main sequence stars that set the confusion limit. This SGR source interpretation appears to gain support from the location of these events in Fig. 9 which indicates that their parallax velocities are among the ones most consistent with Sagittarius Dwarf kinematics.

A rough estimate of the probability of detecting microlensed SGR source stars can be made by noting that SGR Dwarf RR Lyrae stars are about 2.6% as numerous as bulge RR Lyrae in the MACHO fields (Alcock et al. 1997a). In a microlensing parallax sample, we should expect SGR source stars to be enhanced by a factor of  $\sim 20$ , but we must also include both bulge sub-giants and giants in the comparison with the SGR red clump giants. This would reduce the fraction of SGR events by a factor two or so. This would suggest that we might expect that for every 4 microlensing parallax events with bulge giant or sub-giant source we could expect one SGR giant source star event.<sup>2</sup> On the other hand, the ratio of red clump stars to RR Lyrae is likely to be higher for SGR stars than for Galactic bulge stars because of the lower metallicity of SGR, so we might expect fewer SGR events than this RR Lyrae comparison would suggest.

These considerations suggest that we should take the SGR source star hypothesis seriously for these events. However, Cook et al. (2002) used the Keck HIRES spectrograph to obtain spectra of the source stars for these events, and they find radial velocities of  $v_r = -65 \pm 2$  km/s and  $v_r = 64 \pm 2$  km/s for MACHO-98-BLG-6 and MACHO-99-BLG-1, respectively. This is not consistent with the SGR radial velocity (Ibata et al. 1997) of  $v_r = 140 \pm 10$  km/s, and they are about  $2\sigma$  away from the expectation for a disk source star (Wielen 1982). Thus, these events are most likely to have bulge sub-giant source stars.

## 5.5. Likelihood Distance and Mass Estimates

Another, somewhat more general, constraint on  $x$  and  $M$  can be obtained if we make use of our knowledge of the velocity distributions of the source and lensing objects, since the likelihood of obtaining the observed value of  $\tilde{v}$  is a strong function of the distance to the lens. For example, if the disk and bulge velocity dispersions were negligible relative to the Galactic rotation velocity, then for disk lenses we would obtain the relation  $\tilde{v} = 200D_\ell/(D_s - D_\ell)$  km/s implying a lens distance of  $D_\ell = D_s\tilde{v}/(\tilde{v} + 200 \text{ km/s})$ . In reality, the random motions of both disk and bulge stars broaden this relationship somewhat, but we can

<sup>2</sup>A previous estimate of lensing rates for SGR source stars has been made by Cseresnjes & Alard (2001) who find a smaller ratio of SGR/bulge source lensing events than our estimate. This is because they do not consider only microlensing parallax events and because they count the much more numerous events with bulge main sequence source stars.

still obtain a useful constraint.

Given the observed  $\tilde{\mathbf{v}}$ , we obtain a likelihood function

$$L(x; \tilde{\mathbf{v}}) \propto \sqrt{x(1-x)} \rho_L(x) \tilde{v}(1-x)^3 \int f_S(\mathbf{v}_S) f_L((1-x)(\mathbf{v}_\odot + \tilde{\mathbf{v}}) + x\mathbf{v}_S) d\mathbf{v}_S, \quad (8)$$

where  $\rho_L$  is the density of lenses at distance  $x = D_\ell/D_s$ , and the integral is over combinations of source and lens velocities giving the observed  $\tilde{\mathbf{v}} \cdot \mathbf{v}_S$ .  $\mathbf{v}_L = (1-x)(\mathbf{v}_\odot + \tilde{\mathbf{v}}) + x\mathbf{v}_S$  are the 2-D source and lens distribution functions (normalized to unity). We assume the same Galactic parameters as in our  $\tilde{v}$  simulations above: a disk velocity dispersion of 30 km/s in each direction, a flat disk rotation curve of 200 km/s, and a bulge velocity dispersion of 80 km/s with no bulge rotation. The density profiles are a standard double-exponential disk and a Han & Gould (1996) barred bulge. For all events, the source is assumed to reside in the bulge, while the lens may be in the disk or the bulge. But for events MACHO-98-BLG-6 and MACHO-99-BLG-1, we also consider the possibility of a SGR Dwarf source star with the lens in the disk or bulge, although this now appears to be ruled out (Cook et al. 2002).

The resulting likelihood functions for  $D_\ell$  is shown as the long-dashed curves in Figs. 11-13, and these are insensitive to specific parameter choices. These likelihood functions also provide a means for estimating the lens masses via the relation (7), which is also plotted in Figs. 11-13. Fig. 14 shows how the mass estimates correlate with the best fit event timescale for the six high signal-to-noise microlensing parallax events as well as four other events of lower signal-to-noise. (The lower signal-to-noise event with the highest mass is MACHO-99-BLG-22/OGLE-1999-BUL-32 which has been presented as a black hole candidate by Mao et al. 2001.)

One common way to interpret likelihood functions is the Bayesian method, in which the lens mass (or distance) probability distribution is given by the likelihood function times a prior distribution, which represents our prior knowledge of the probability distribution. In our case, the likelihood function represents all of our knowledge about the lens mass and location, so we select a uniform prior. With a uniform prior, the likelihood function becomes the probability distribution and we are able to calculate the lens mass confidence levels listed in Table 3. This table also includes lens mass confidence levels for models that differ from the preferred model in order to show how the mass estimates depend upon the amount of blending (for MACHO-96-BLG-5) and on whether the source star resides in the Galactic bulge or the SGR Dwarf. Note that the uncertainty in the mass estimates is smaller for SGR Dwarf sources due to the small velocity dispersion of the SGR Dwarf and the smaller range of likely lens distances.

## 5.6. Constraints on Main Sequence Lenses

If we assume that the lens stars are main sequence stars, then we can obtain an additional constraint on their distances and masses by comparing the brightness of a main sequence star, of the implied mass, to the upper limit on the brightness of the lens star. We have assigned a conservative upper limit on the V-band brightness of each lens star based upon the available photometry and microlensing parallax fits listed in Table 2. In the case of MACHO-96-BLG-5, the upper limit is particularly stringent because it is based upon

HST observations. Note that if we assign some of the flux of the star identified in the HST images to the lens star instead of the source, the best fit  $\hat{t}$  will increase almost linearly with the inverse of the source star flux. This causes the lens mass estimate to increase as  $\sim \hat{t}^2$ . Since stellar luminosity varies as a high power of the mass, a main sequence lens will be more strongly ruled out.

In order to apply these constraints to the likelihood functions for the mass and distances of the lens stars, we have multiplied the likelihood function by the Gaussian probability that the lens brightness exceeds the upper limit on the brightness of lens star. This gives the short-dashed likelihood curves shown in Figs. 11-13. These results are insensitive to our assumed  $L \propto M^4$  mass-luminosity relation. The properties of the most likely main sequence lens models are given in Table 4, which is discussed in more detail in section 6.2. An important parameter in this table is the predicted lens-source separation in June, 2003. This can be calculated from the lens-source proper motion which is related to the projected velocity by  $\mu = \tilde{v}(D_s - D_\ell)/(D_s D_\ell)$ .

### 5.7. Stellar Remnant Lenses and Black Hole Candidates

The mean mass estimate for the six microlensing parallax events is  $2.7M_\odot$ . Five of the six have best fit masses  $> 1M_\odot$ , and two of the events, MACHO-96-BLG-5 and MACHO-98-BLG-6, have best fit masses  $> 3M_\odot$ . This makes them black hole candidates because the maximum neutron star mass is thought to be  $\sim 2M_\odot$  (Akmal, Pandharipande, & Ravenhall 1998). The 95% confidence level lower limits on the masses of these lenses are  $1.64M_\odot$  and  $0.94M_\odot$ , respectively, while the 90% confidence level lower limits are  $2.3M_\odot$  and  $1.9M_\odot$ . A main sequence star lens at the lower limit mass is strongly excluded in the case of MACHO-96-BLG-5 because of the constraint on the lens brightness from HST images. However, a main sequence lens with a mass at the 95% confidence limit is not quite excluded for MACHO-98-BLG-6. The masses that have been measured for neutron stars are close to the Chandrasekhar mass,  $M_{NS} = 1.35 \pm 0.04M_\odot$  (Thorsett & Chakrabarty 1999), which is excluded at better than 95% confidence for MACHO-96-BLG-5 and better than 90% confidence for MACHO-98-BLG-6. Thus, both MACHO-96-BLG-5 and MACHO-98-BLG-6 are both black hole candidates, but there is a small chance that MACHO-98-BLG-6 could be a neutron star or even a main sequence star.

In addition to these black hole candidates, three of the remaining four microlensing parallax events have best fit masses  $> 1M_\odot$ . For MACHO-104-C and MACHO-96-BLG-12, main sequence lens are disfavored, but not ruled out. MACHO-99-BLG-8 appears to be blended with a relatively bright source, so a main sequence lens of  $M \gtrsim M_\odot$  is a possibility. As we explain below, with HST imaging it will be straightforward to detect the lenses if they are main sequence stars. If HST images fail to detect the lens stars, then we can show that the lenses are almost certainly stellar remnants.

## 6. Follow-up Observations

The detection of the microlensing parallax effect allows us to make a lens mass estimate that is accurate to about a factor of two, and to identify the black hole candidates. However, these estimates are not accurate

enough to determine the black hole mass function, and they do not allow the unambiguous identification of neutron star or white dwarf lenses. However, follow-up observations with higher resolution instruments hold the promise of much more precise determinations of the lens masses.

### 6.1. Interferometric Follow-up

The most ambitious of microlensing event follow-up plans involve interferometric instruments such as the Keck and VLT interferometers (Delplancke, Górska & Richichi 2001) and the Space Interferometry Mission (SIM) (Boden, Shao, & van Buren 1998). The most spectacular confirmation of a black hole event would be to measure the image splitting which is given by

$$\phi_{\text{sep}} = 2\theta_E \sqrt{1 + u^2/4}, \quad (9)$$

where  $\theta_E$  is the image separation and  $u$  is given by eq. (3). For MACHO-96-BLG-5, we have  $\theta_E = 9.8$  mas if the lens is at the distance preferred by the likelihood analysis. This compares to the 5 mas diffraction limit of an interferometer with a 100 m baseline operating at a wavelength of  $2\mu\text{m}$ , such as the Keck or VLT Interferometers. In fact, these instruments are expected to be able to measure image splittings as small as  $\sim 30\mu\text{as}$  (Delplancke, Górska & Richichi 2001). Such measurements would allow a direct measurement of the lens mass:

$$M = \frac{\tilde{v}t\theta_E c^2}{8G}. \quad (10)$$

The most challenging aspect of such measurements is the faintness of source stars such as the MACHO-96-BLG-5 source, which is close to the (rather uncertain) magnitude limit of the VLT Interferometer (Delplancke, Górska & Richichi 2001).

Even if the images cannot be resolved, it may be possible to measure the deflection of the image centroid (Hog, Novikov, & Polnarev 1995; Miyamoto & Yoshi 1995; Walker 1995) which is given by

$$\Delta\phi = \left( \frac{u^2 + 3}{\sqrt{u^2 + 4}} - u \right) \theta_E. \quad (11)$$

This can be measured by a very accurate astrometry mission such as SIM (Boden, Shao, & van Buren 1998; Paczyński 1998; Gould 2000). Once again, however, the MACHO-96-BLG-5 source is a rather faint target for SIM, but in this case, the measurement is not so difficult because the amplitude of the centroid motion is very much larger than SIM's sensitivity limit.

If it should turn out that some of the more massive lenses are located very close to us, then it might be possible to directly observe the lensed images with HST. This is a realistic possibility for the MACHO-99-BLG-22/OGLE-1999-BUL-32 event (Mao et al. 2001) because its  $\tilde{v}$  value is in the opposite quadrant from the events studied in this paper. This gives a likelihood function with two peaks: one at a distance of  $\sim 500\text{pc}$  for a lens in the disk and one at a distance of  $\sim 6\text{kpc}$  for a bulge lens (Bennett et al. 2001). The bulge lens solution predicts a mass of a few  $M_\odot$ , but the disk lens solution predicts a mass of  $> 100M_\odot$  and a lensed image separation of  $\sim 0.1''$ .

## 6.2. Lens Detection and Source Proper Motion

Another method can be used to make a direct determination of the lens mass for a bright lens star. If the lens can be detected and the relative proper motion of the lens with respect to the source is measured, then it is also possible to determine the lens mass from the proper motion and microlensing parallax parameters with the following formula:

$$M = \frac{\tilde{v} \hat{t}^2 \mu c^2}{16G}, \quad (12)$$

where  $\mu$  is the relative lens–source proper motion. This technique has the advantage that the proper motion measurements can be made many years after the peak magnification of the microlensing event. The lens–source separation can reach the 50–100 mas range within 5–10 years. Table 4 shows the predicted separations and lens brightness contrasts for our six strong microlensing parallax events. The columns are (1) the MACHO event name, (2) the lens mass with  $1\sigma$  errors, (3) a likely lens mass,  $M_{rmMS}$ , if the lens is on the main sequence, (4) the lens distance,  $D_{\ell-MS}$  for a lens of mass  $M_{rmMS}$ , (5) the predicted lens–source separation in June, 2003, (6) the apparent V magnitude of the lenses, and (7–11) the predicted contrast between the lens and source brightness in the UBV<sub>I</sub> bands. Positive  $\Delta$ -mags. imply that the source is brighter than the lens, so lens detection is easiest for events that have small or negative  $\Delta$ -mag. values. With the exceptions of MACHO-96-BLG-5, which doesn't have a viable main sequence lens model, all of the other lens stars should be detectable if they are not stellar remnants.

When the lens can be detected, it should also be possible to constrain the unlensed brightness of the source star, which will reduce the error bars on  $\hat{t}$ . Also, it should be possible to get very accurate measures of the relative proper motion,  $\mu$ , as the lens moves further from the source. Thus, the ultimate limits on the masses of the lenses may come from the uncertainties in the  $\tilde{v}$  values, which range from 2 – 10 %.

When the lenses are undetectable, it should still be possible to measure the proper motion of the source star with HST images separated by  $\sim 5$  years. The proper motion can only be measured with respect to the average of other, nearby stars because extra-galactic reference sources are not easily identified in these crowded Galactic bulge fields (Spaenhauer, Jones, & Whitford 1992; Zoccali et al. 2001). Proper motion measurements of the microlensed source stars would allow us to remove one degree of freedom from our likelihood analysis and reduce the uncertainty in the implied lens distances and masses. The proper motion distribution of the stars in the same field will also allow us to test the Galactic models that are used for the likelihood analysis, and so this should reduce the systematic uncertainties in the lens distance and mass estimates.

## 7. Conclusions

We have performed microlensing parallax fits on the Galactic bulge events detected by the MACHO Collaboration with timescales of  $\hat{t} \geq 140$  days, and found six events with highly significant detections of the microlensing parallax effect. Our analysis of the velocity distributions expected for parallax microlensing events from different source star populations suggests that source stars in the SGR Dwarf Galaxy might

contribute to the detectable microlensing parallax events, and inspection of the source star color-magnitude diagrams indicates that two of our microlensing parallax events have source stars which could be SGR Dwarf red clump stars. However, radial velocity measurements (Cook et al. 2002) indicate that they are probably bulge sub-giant stars.

A likelihood analysis has been employed to estimate the distance and masses of the lenses, and this indicates an average mass for our six lenses of  $2.7 M_{\odot}$ . Two of the lenses have masses large enough to imply that they are probably massive stellar remnants: The mass estimates for the MACHO-96-BLG-5 and MACHO-98-BLG-6 lenses are  $M/M_{\odot} = 6^{+10}_{-3}$  and  $M/M_{\odot} = 6^{+7}_{-3}$ , respectively, which implies that both are likely to be black holes. Together with MACHO-99-BLG-22/OGLE-1999-BUL-32 (Mao et al. 2001), these are the first black hole candidates that are truly black since we have not seen any radiation from matter that is gravitationally bound to the black hole.

Similar events detected in the next few years may yield lens masses that are measured much more precisely due to follow-up observations from ground-based (Delplancke, Górska & Richichi 2001) and space-based (Gould 2000) interferometers. This will allow an unambiguous determination of the abundance and mass function of black hole and neutron star stellar remnants, although it may be difficult to determine if  $\sim 2 M_{\odot}$  objects are black holes or neutron stars. At present, there are three black hole microlens candidates in the sample of 321 microlensing events that was the starting point for this paper (although MACHO-99-BLG-22 is only identified as a strong black hole candidate when OGLE data are included in the analysis (Mao et al. 2001)). This is about 1% of the events, but far more than 1% of the total contribution to the microlensing optical depth. This might seem to suggest that the fraction of our Galaxy’s stellar mass that is in the form of black holes is much larger than 1%. However, we have not made an accurate determination of our efficiency for discovering microlensing events when a strong microlensing parallax effect is present. The non-linear projected velocity of such events is likely to result in an enhanced detection probability, but this effect has not been studied. Given the small number of events, and the significant possibility that one of the three may not be a black hole, it is safe to conclude that our results are consistent with models which predict that of order 1% of the Milky Way’s stellar mass should be in the form of black holes (Brown & Bethe 1994; Fryer & Kalogera 2001; Gould 2000). If all three of these events are truly due to black hole lenses, then a black hole mass fraction somewhat higher than 1% might be preferred. These results appear to indicate that most stellar mass black holes do not reside in the X-ray binary systems where they are most easily observed (Bailyn, Jain, Coppi, & Orosz 1998).

This work was supported, in part, by NASA through the Space Telescope Science Institute (GO 8490) and through the NASA Origins Program (NAG5-4573). It was also supported by the National Science Foundation grants program (AST96-19575), and through the Office of Science and Technology Centers (AST-8809616). DM is supported by Fondecyt 1990440. CWS thanks the Packard Foundation for the generous support. WJS is supported by a PPARC Advanced Fellowship. CAN is supported in part by a NPSC Graduate Fellowship. TV and KG were supported in part by the DOE.

## REFERENCES

Afonso, C., et al. 2000, *ApJ*, 532, 340

Akmal, A., Pandharipande, V. R., & Ravenhall, D. G. 1998, *Phys.Rev. C* 58, 1804

Alcock, C., et al. 1993, *Nature*, 365, 621

Alcock, C., et al. 1995, *ApJ*, 454, L125

Alcock, C., et al. 1996, *ApJ*, 463, L67

Alcock, C., et al. 1997a, *ApJ*, 474, 217

Alcock, C., et al. 1997b, *ApJ*, 479, 119; (E) 500, 522

Alcock, C., et al. 1997c, *ApJ*, 491, 436

Alcock, C., et al. 1999, *PASP*, 111, 1539

Alcock, C., et al. 2001a, *ApJ*, 552, 259

Alcock, C., et al. 2001b, *ApJ*, 552, 582

Aubourg, E. et al. 1993, *Nature*, 365, 623

Bailyn, C. D., Jain, R. K., Coppi, P., & Orosz, J. A. 1998, *ApJ*, 499, 367

Becker, A. C. 2000, PhD thesis, University of Washington

Bennett, D. P. et al. 1993, American Astronomical Society Meeting, 183, 7206

Bennett, D. P., et al. 1996, *Nucl. Phys. B* (Proc. Suppl.), Vol. 51B, 131

Bennett, D. P., et al. 2001, in preparation.

Boden, A. F., Shao, M., & van Buren, D. 1998, *ApJ*, 502, 538

Bond, I., et al. 2001, *MNRAS*, in press (astro-ph/0102181).

Brown, G. E. & Bethe, H. A. 1994, *ApJ*, 423, 659

Cook, K., et al. 2002, in preparation

Cseresnjes, P. & Alard, C. 2001, *A&A*, 369, 778

Dehnen, W. & Binney, J. J. 1998, *MNRAS*, 298, 387

Delplancke, F., Górska, K. M. & Richichi, A. 2001, *A&A*, in press (astro-ph/0108178)

Derue et al. 1999, *A&A*, 351, 87

Fruchter, A. & Hook, R. N. 1997, Proc. SPIE, 3164, 120

Fryer, C. L. & Kalogera, V. 2001, ApJ, 554, 548

Gould, A. 1992, ApJ, 392, 442

Gould, A. 2000, ApJ, 535, 928

Griest, K. & Hu, W. 1993, ApJ, 407, 440

Han, C. & Gould, A. 1996, ApJ, 467, 540

Han, C. & Gould, A. 1997, ApJ, 480, 196

Hog, E., Novikov, I. D., & Polnarev, A. G. 1995, A&A, 294, 287

Holtzman, J. A., Watson, A. M., Baum, W. A., Grillmair, C. J., Groth, E. J., Light, R. M., Lynds, R., & O’Neil, E. J. 1998, AJ, 115, 1946

Ibata, R. A., Wyse, R. F. G., Gilmore, G., Irwin, M. J., & Suntzeff, N. B. 1997, AJ, 113, 634

Liebes, S. 1964, Physical Review , 133, 835

Mao, S. 1999, A&A, 350, L19

Mao, S. et al. 2001, MNRAS, submitted (astro-ph/0108312)

Minniti, D. 1996, ApJ, 459, 175

Miyamoto, M. & Yoshi, Y. 1995, AJ, 110, 1427

Nemiroff, R. J. & Wickramasinghe, W. A. D. T. 1994, ApJ, 424, L21

Paczyński, B. 1986, ApJ, 304, 1

Paczyński , B. 1998, ApJ, 494, L23

Refsdal, S. 1966, MNRAS, 134, 315

Rhie, S. H., Becker, A. C., Bennett, D. P., Fragile, P. C., Johnson, B. R., King, L. J., Peterson, B. A., & Quinn, J. 1999, ApJ, 522, 1037

Schechter, P. L., Mateo, M., & Saha, A. 1993, PASP, 105, 1342

Smith, M. C., Mao, S., & Woźniak, P. 2001, MNRAS, submitted.

Soszyński, I. et al. 2001, ApJ, 552, 731

Spaenhauer, A., Jones, B. F., & Whitford, A. E. 1992, AJ, 103, 297

Stetson, P. B. 1987, PASP, 99, 191

Stetson, P. B. 1994, PASP, 106, 250

Thorsett, S. E. & Chakrabarty, D. 1999, ApJ, 512, 288

Tomaney, A. B. & Croots, A. P. S. 1996, AJ, 112, 2872

Udalski, A., Szymański, M., Kałużny, J., Kubiak, M., Krzmiński, W., Mateo, M., Preston, G. W., & Paczyński , B. 1993, Acta Astronomica, 43, 289

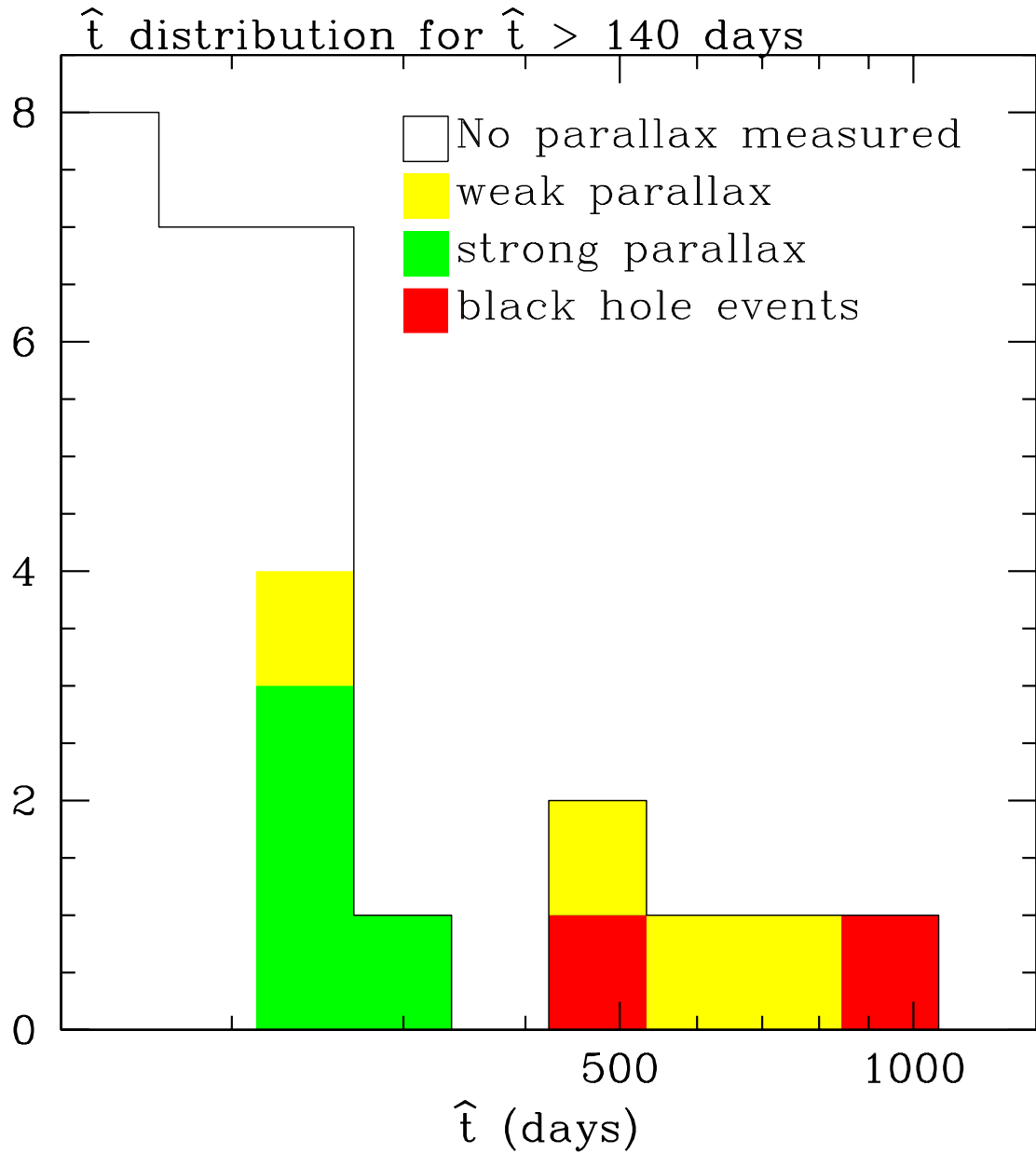
Udalski, A. et al. 1994a, Acta Astronomica, 44, 165

Udalski, A., Szymański, M., Kałużny, J., Kubiak, M., Mateo, M., Krzmiński, W., & Paczyński , B. 1994b, Acta Astronomica, 44, 227

Walker, M. A. 1995, ApJ, 453, 37

Wielen, M. A. 1982, Landolt-Börnstein Tables, Astrophys., 2C, Sec. 8.4, 202

Zoccali, M., Renzini, A., Ortolani, S., Bica, E., & Barbuy, B. 2001, AJ, 121, 2638



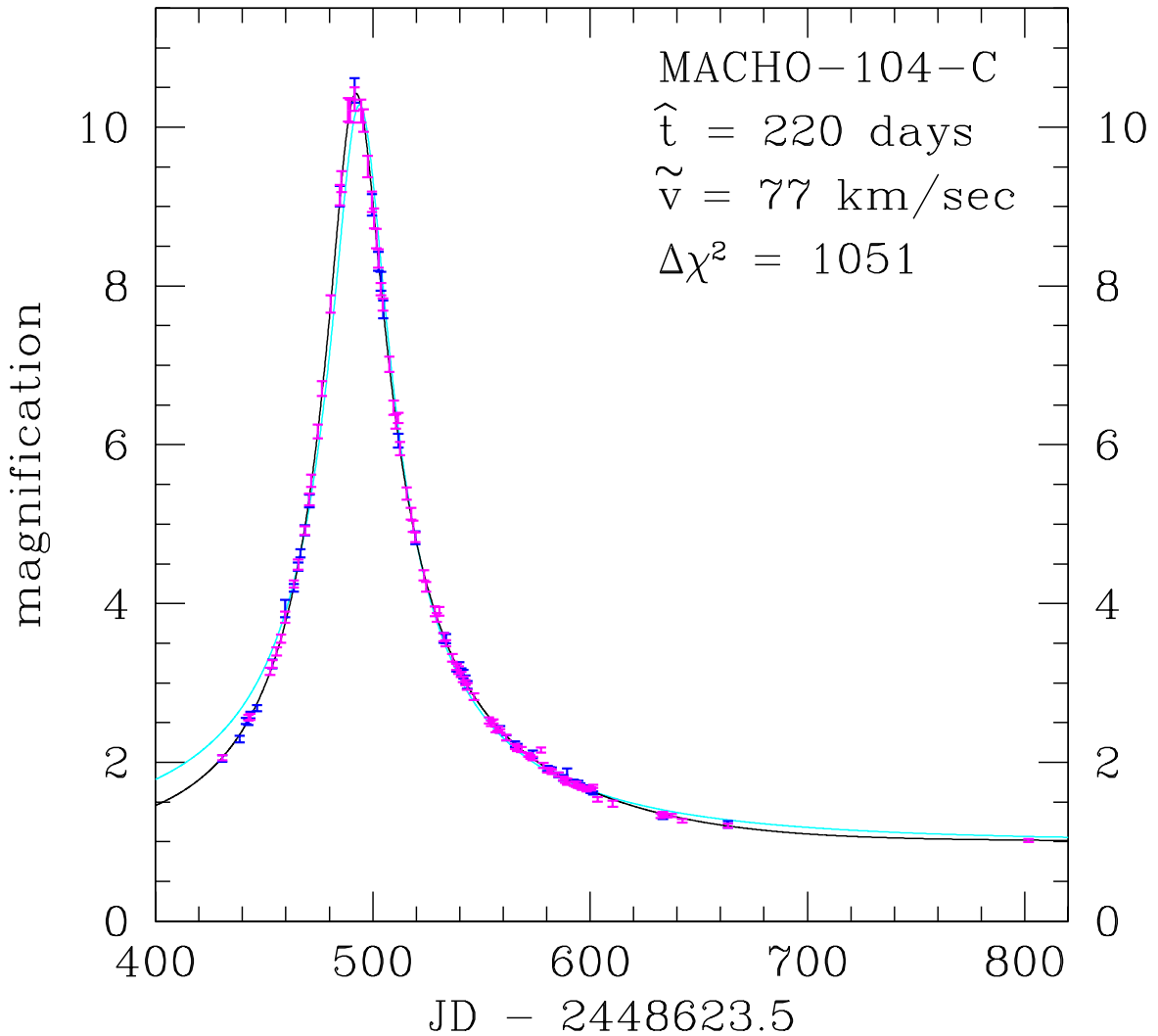


Fig. 2.— MACHO-104-C light curves normalized to the unlensed flux of the lensed star. The MACHO red and blue data are plotted in magenta and blue, respectively. The black curve is the parallax fit while the cyan curve is the best fit standard microlensing lightcurve. An additional 5 years of data showing no photometric variation are not shown.

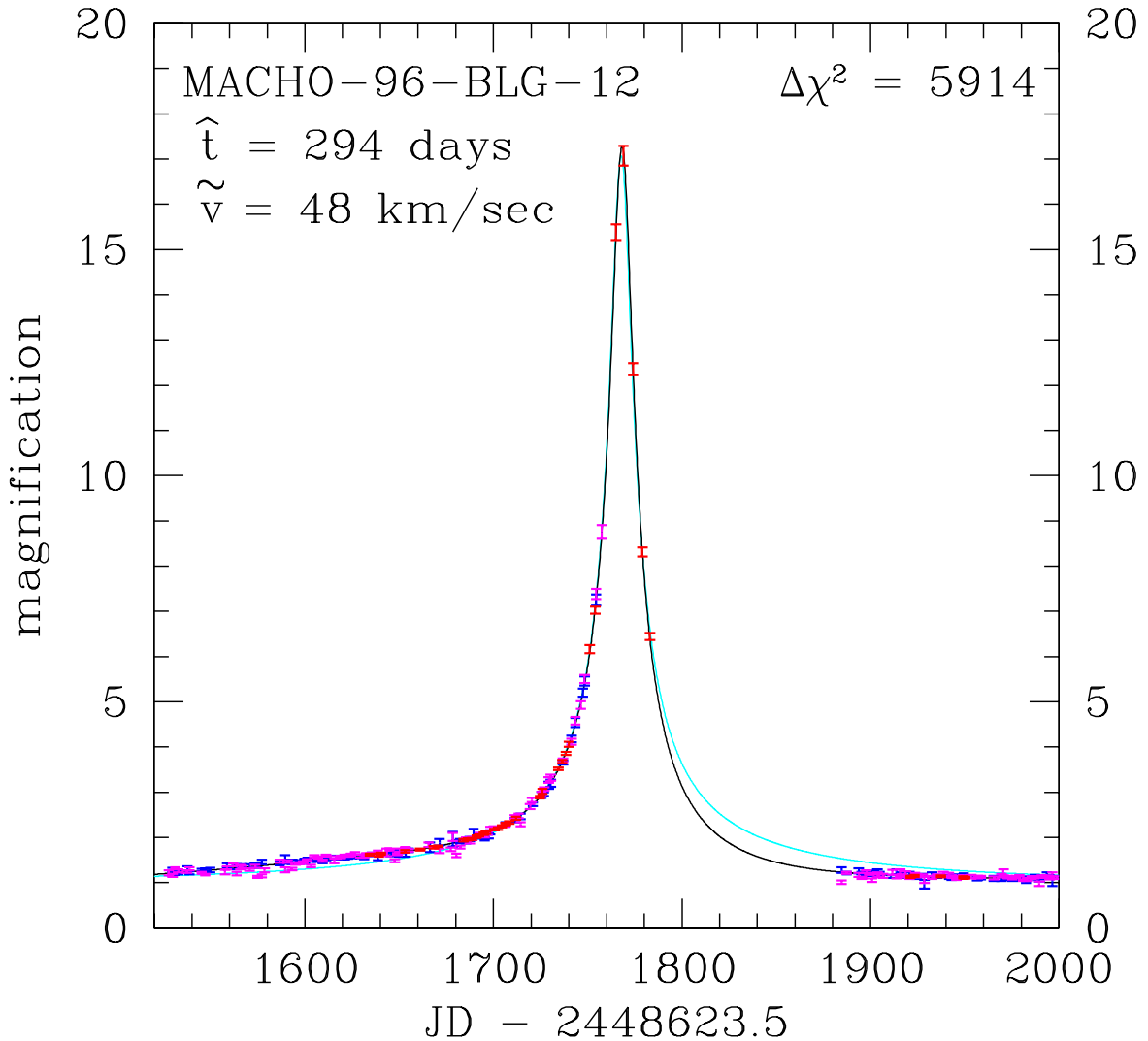


Fig. 3.— MACHO-96-BLG-12 lightcurve closeup with lightcurves normalized to the unlensed flux of the lensed star. The MACHO red and blue data are plotted in magenta and blue, respectively, and the CTIO data are shown in red. The black curve is the parallax fit while the cyan curve is the best fit standard microlensing lightcurve. An additional 5 years of data showing no photometric variation are not shown.

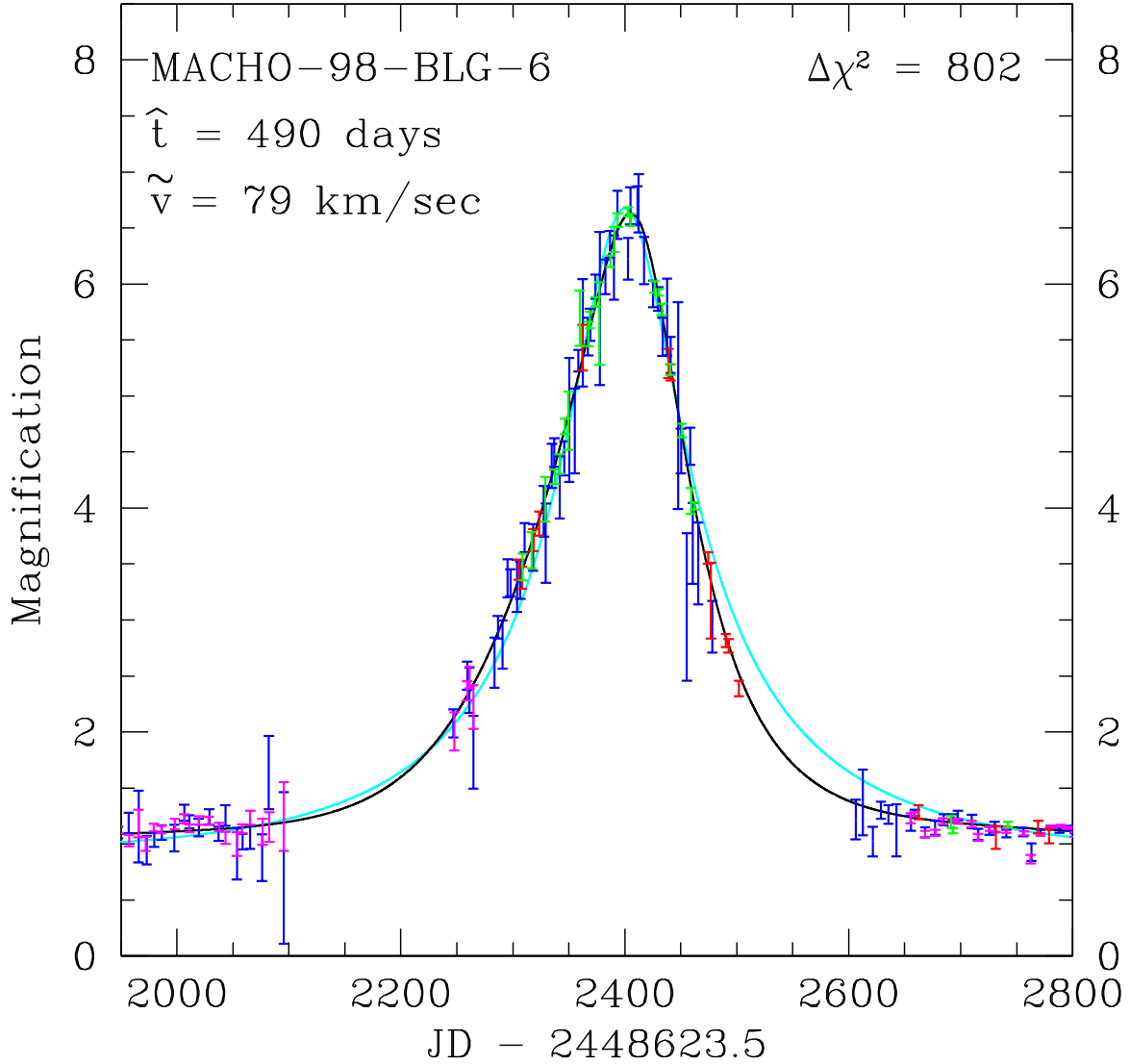


Fig. 4.— MACHO-98-BLG-6 lightcurve closeup with lightcurves normalized to the unlensed flux of the lensed star. The MACHO red and blue data are plotted in magenta and blue, respectively, the CTIO data are shown in red, and the MPS data are shown in green. The black curve is the parallax fit while the cyan curve is the best fit standard microlensing lightcurve. The gap in the MACHO red data during the day 2280-2650 interval is due to a CCD failure. An additional year of data showing no photometric variation is not shown.

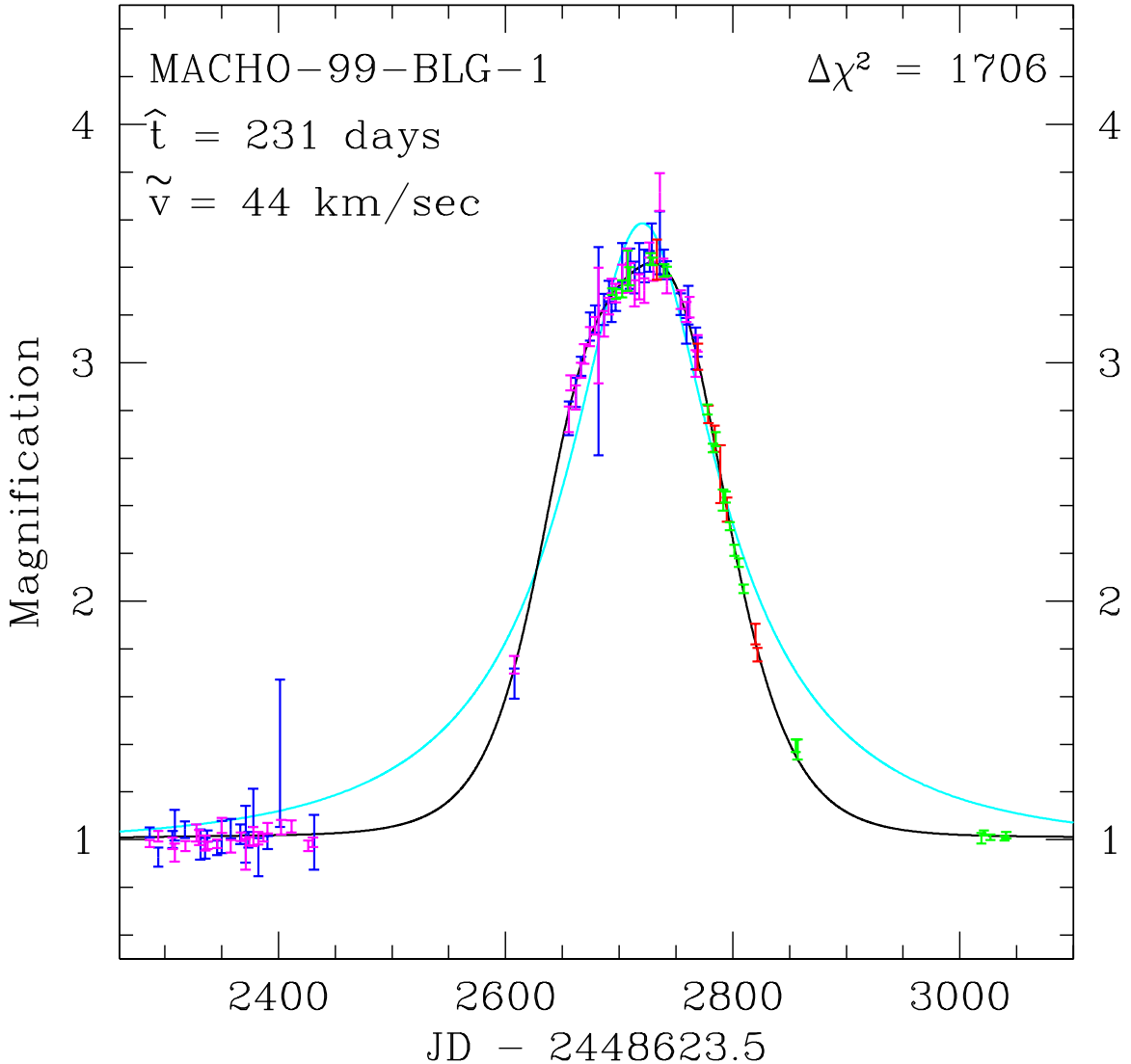


Fig. 5.— MACHO-99-BLG-1 light curves normalized to the unlensed flux of the lensed star. The MACHO red and blue data are plotted in magenta and blue, respectively, the CTIO data are shown in red, and the MPS data are shown in green. The black curve is the parallax fit while the cyan curve is the best fit standard microlensing lightcurve. An additional 4 years of data showing very little photometric variation are not shown.

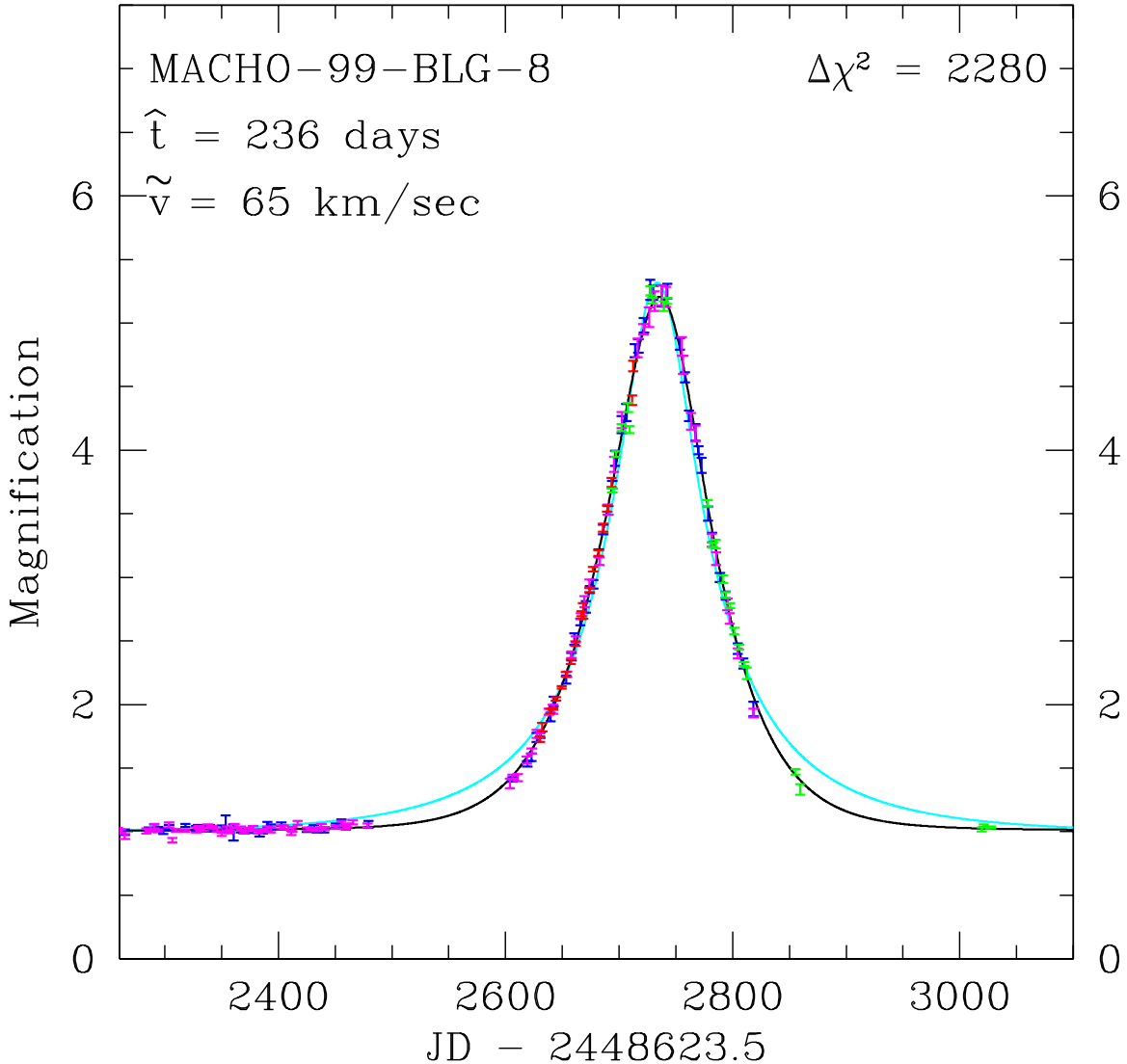


Fig. 6.— MACHO-99-BLG-8 light curves normalized to the unlensed flux of the lensed star. The MACHO red and blue data are plotted in magenta and blue, respectively, the CTIO data are shown in red, and the MPS data are shown in green. The black curve is the parallax fit while the cyan curve is the best fit standard microlensing lightcurve. An additional 3 years of data showing very little photometric variation are not shown.

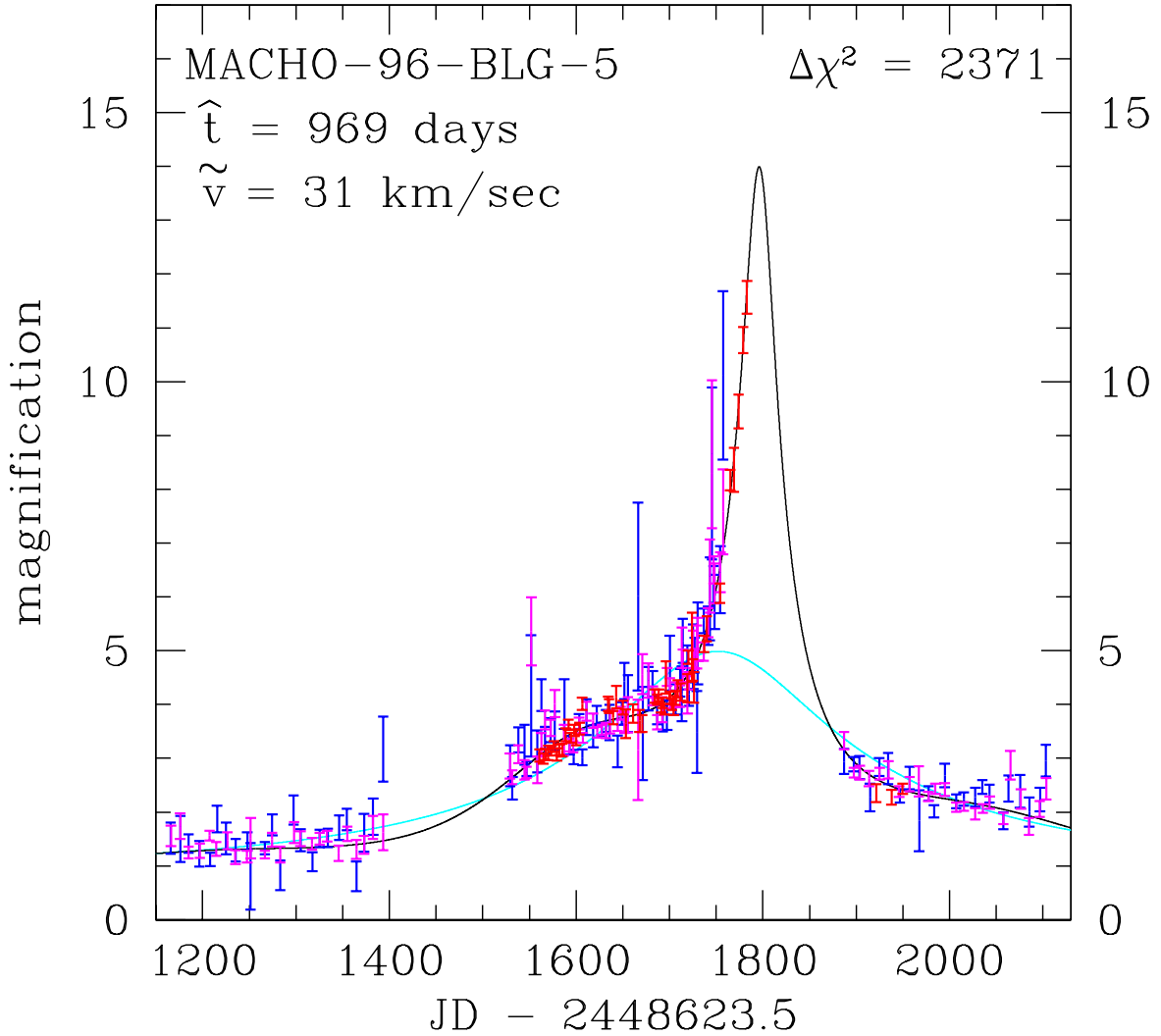


Fig. 7.— MACHO-96-BLG-5 lightcurves normalized to the unlensed flux of the lensed star. The MACHO red and blue data are plotted in magenta and blue, respectively, and the CTIO data are shown in red. The black curve is the parallax fit while the cyan curve is the best fit standard microlensing lightcurve. An additional 4 years of data showing very little photometric variation are not shown.

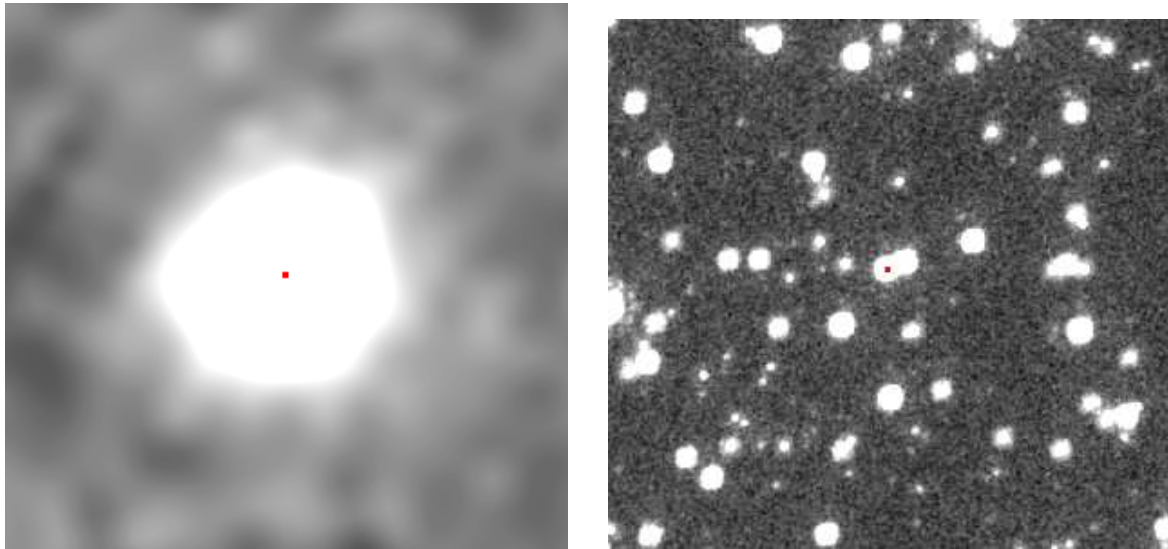


Fig. 8.— The image on the left is the master difference image as described in the text. It has been registered to the same coordinate system as the F814W HST/WFPC2 image shown on the right. The red marks show the centroid of the variable flux in the master difference image and the location of this centroid when transformed to the coordinate system of the HST data. A single, main sequence bulge star is clearly identified as the lensed source star.

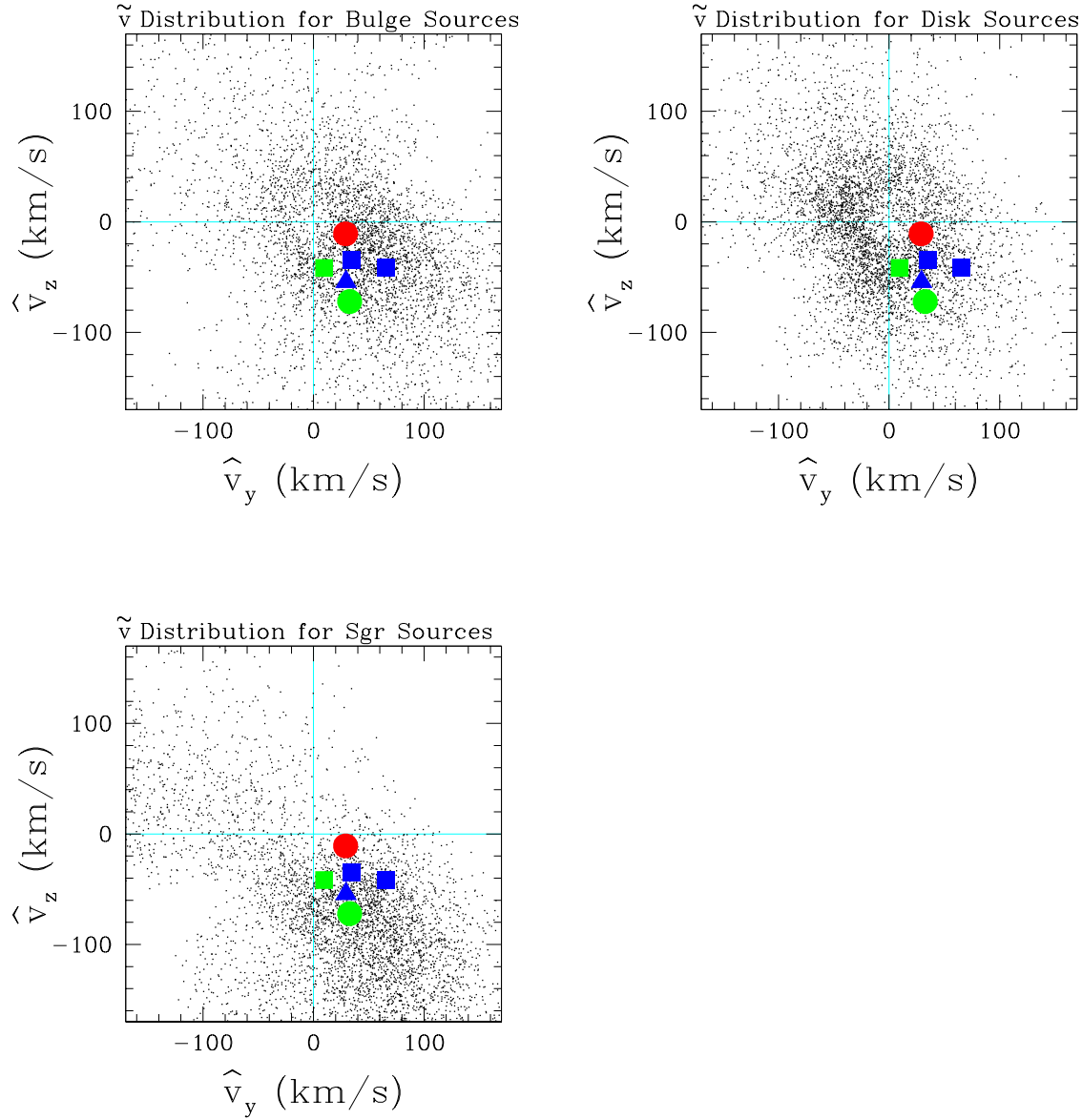
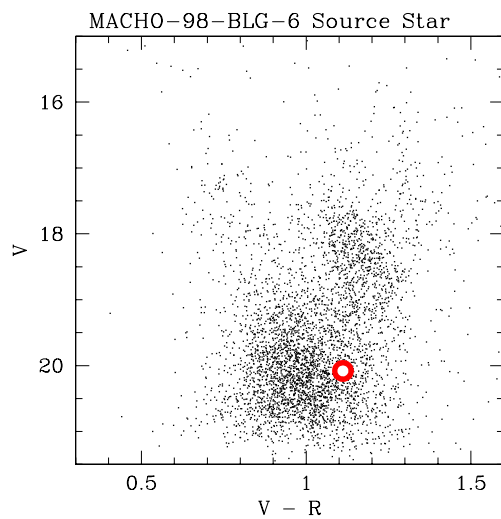
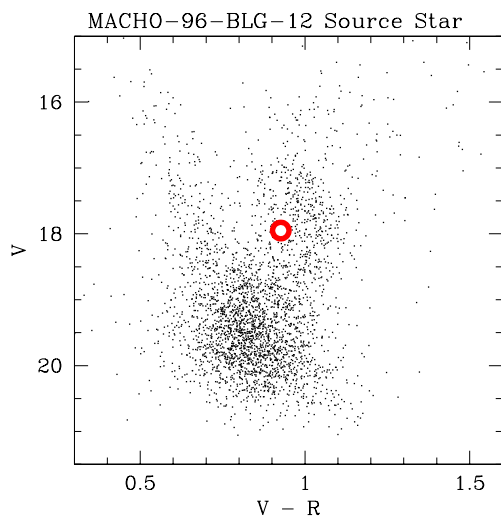
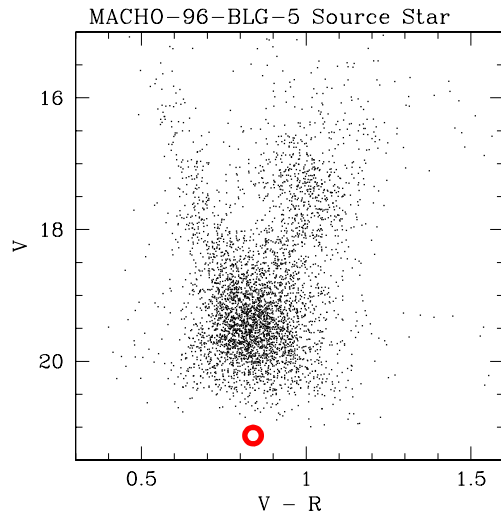
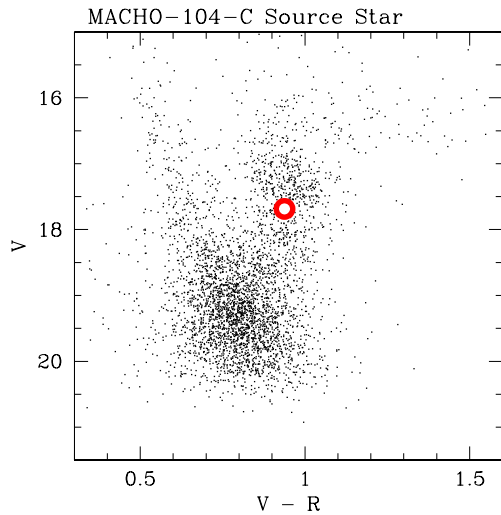


Fig. 9.— The distribution of  $\tilde{v}$  values in Galactic coordinates is shown for simulated microlensing parallax events towards the Galactic bulge for three different source star populations: the Galactic bulge, the foreground Galactic disk, and the Sagittarius Dwarf Galaxy. The large colored dots show the locations of our detected microlensing parallax events. The red circular spot is our best black hole candidate, MACHO-96-BLG-5, and the green circular disk is the other black hole candidate: MACHO-98-BLG-6. The two green spots are the events with source stars that appear to be bulge sub-giants or Sagittarius Dwarf red clump stars. (MACHO-99-BLG-1 is the other). The blue squares are the bulge red clump source star events, and the blue triangle is MACHO-98-BLG-8 which has a red giant source and is probably also in the bulge.



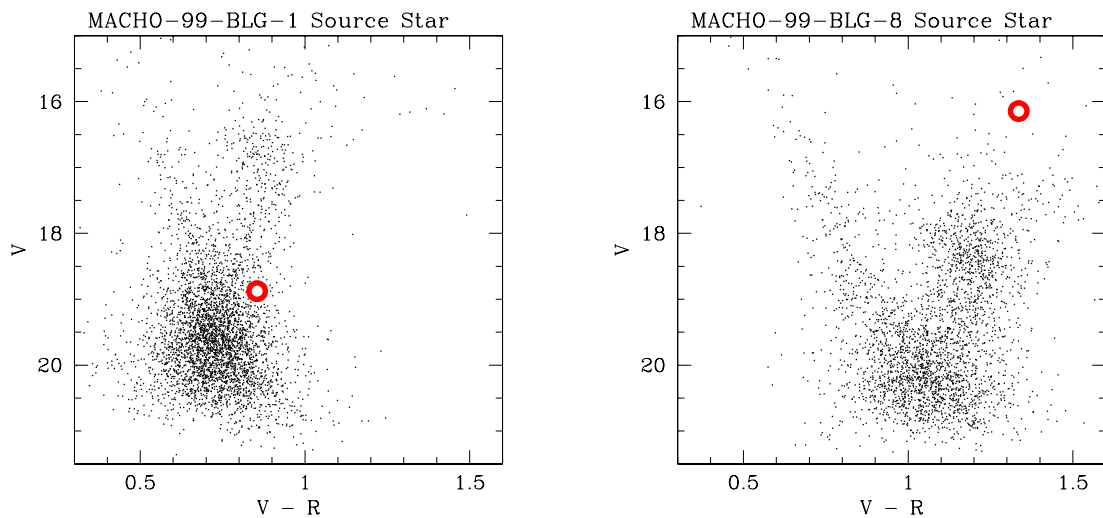


Fig. 10.— Color-Magnitude diagrams from MACHO data are shown for all the detected stars within a 2 arc minute circle around each of our microlensing parallax events. The red circles indicate the location of the lensed source star, assuming the blending implied by the microlensing parallax fits.

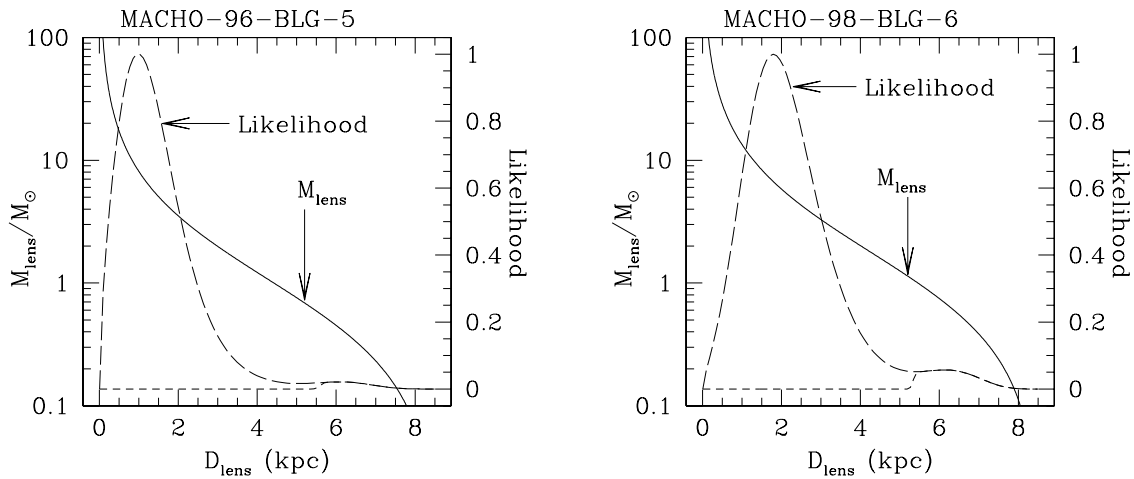


Fig. 11.— The mass vs. distance relations (solid curves) for our candidate black hole lenses are shown along with the likelihood functions (long dashed curves) computed assuming a standard model for the Galactic phase space distribution. The source star is assumed to reside in the bulge for both events. The implied best fit masses are  $M = 6^{+10}_{-3} M_{\odot}$  for the MACHO-96-BLG-5 lens and  $M = 6^{+7}_{-3} M_{\odot}$  for the MACHO-98-BLG-6. The 95% confidence level lower limits on the masses are  $1.6 M_{\odot}$  and  $0.94 M_{\odot}$  respectively. The short dashed curves show likelihood functions including the constraint on the brightness of a main sequence lens star. For MACHO-96-BLG-5, the upper limit on the lens brightness is very stringent because of the HST images, and a main sequence lens is ruled out.

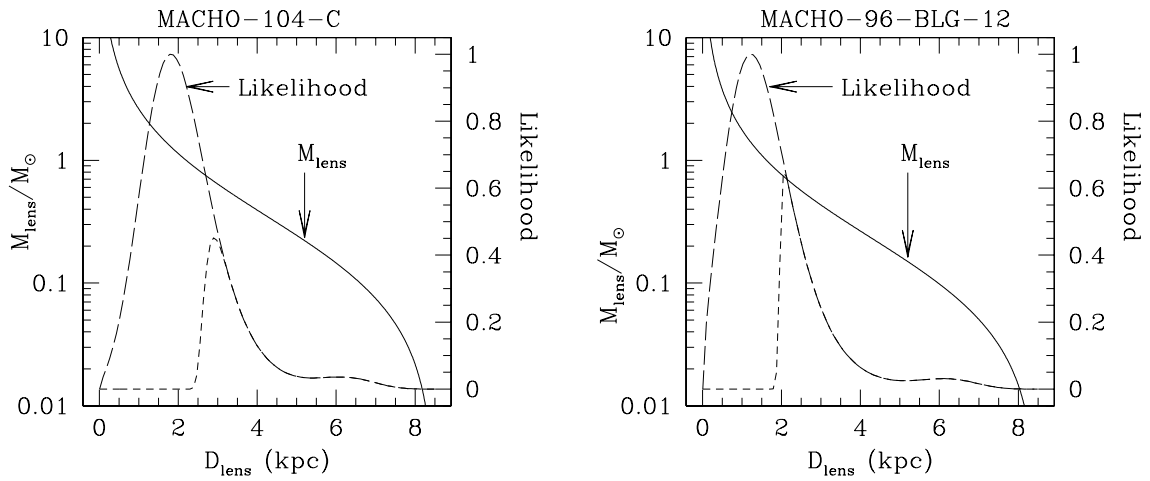


Fig. 12.— The mass vs. distance relations (solid curves) for our two bulge clump giant source events are shown along with the likelihood functions (long dashed curves) computed assuming a standard model for the Galactic phase space distribution. The implied best fit masses are  $M = 1.1_{-0.5}^{+1.1} M_{\odot}$  for the MACHO-104-C lens and  $M = 1.3_{-0.7}^{+1.8} M_{\odot}$  for the MACHO-96-BLG-12. The 95% confidence level lower limits on the masses are  $0.35 M_{\odot}$  and  $0.33 M_{\odot}$  respectively. The short dashed curves show likelihood functions including the constraint on the brightness of a main sequence lens star, and they indicate that main sequence lenses are disfavored but not ruled out.

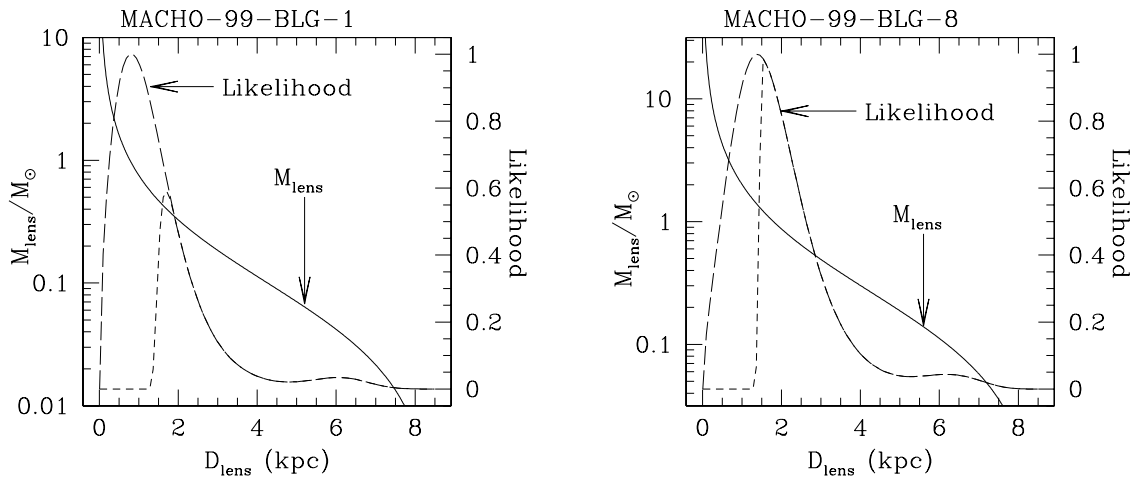


Fig. 13.— The mass vs. distance relations (solid curves) for the two 1999 microlensing parallax events are shown along with the likelihood functions (long dashed curves) computed assuming a standard model for the Galactic phase space distribution. For both events the source star is assumed to reside in the Galactic bulge. The implied best fit masses are  $M = 0.7_{-0.4}^{+1.2} M_{\odot}$  for the MACHO-99-BLG-1 lens and  $M = 1.2_{-0.6}^{+1.6} M_{\odot}$  for the MACHO-99-BLG-8. The 95% confidence level lower limits on the masses are  $0.14 M_{\odot}$  and  $0.3 M_{\odot}$  respectively. The short dashed curves show likelihood functions including the constraint on the brightness of a main sequence lens star, and these indicate that the lens brightness constraints are consistent with main sequence lens stars. For MACHO-99-BLG-1, a main sequence lens is disfavored, however.

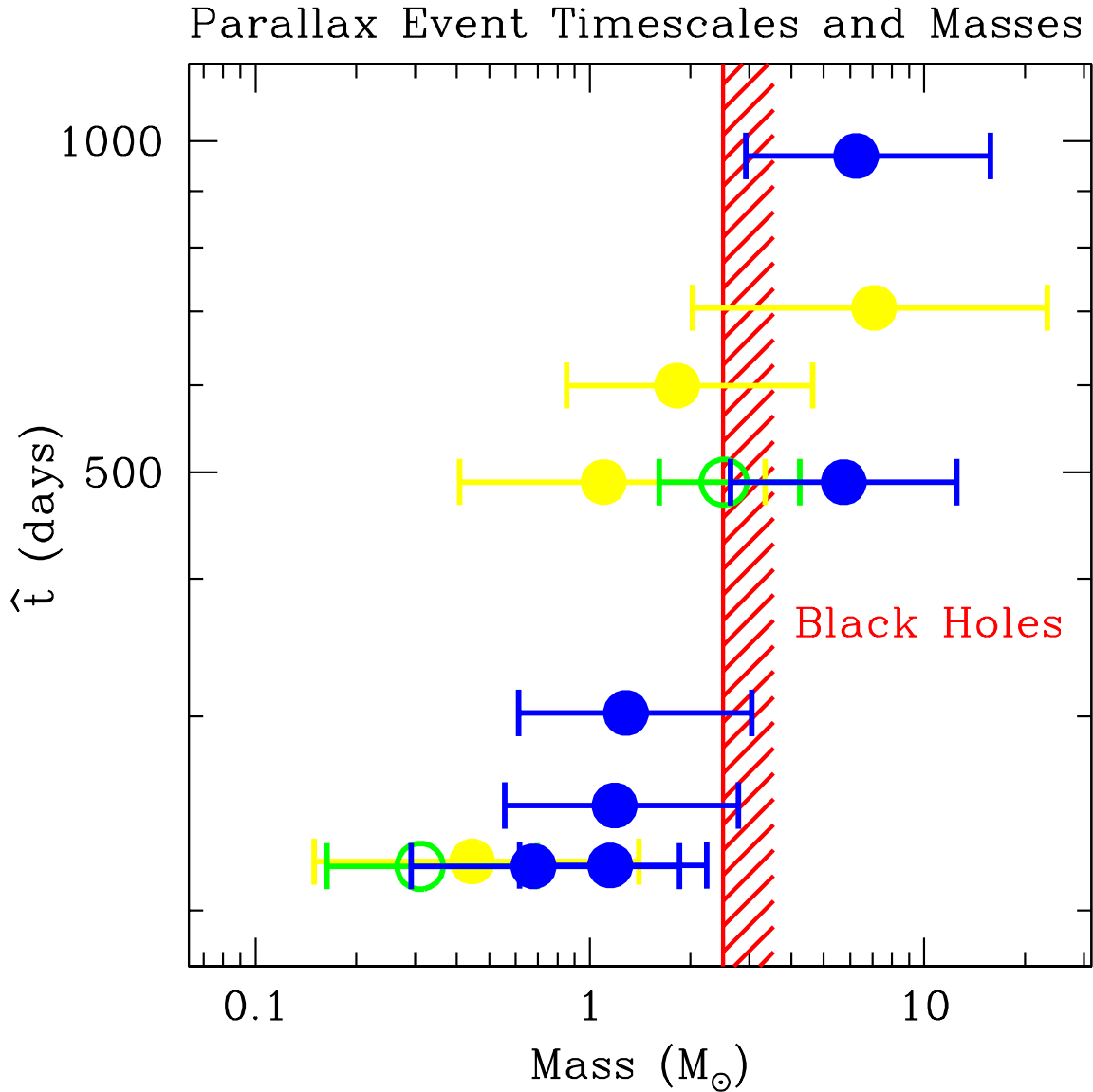


Fig. 14.— This plot shows  $M$  vs.  $\hat{t}$  for the 10 events with  $\hat{t} > 140$  days with  $1\sigma$  error bars for the mass estimates. All events with formally significant detections of microlensing parallax are shown, but parallax signal for the events indicated in yellow is weak enough that the detection is not considered to be definitive. The green open symbols indicate the predicted lens masses for MACHO-98-BLG-6 and MACHO-99-BLG-1 if their source stars were in the SGR Dwarf Galaxy, a possibility that appears to be contradicted by their spectra.

Table 1. Microlensing Parallax Event Coordinates

Event Name	MACHO Star ID	RA(J2000)	DEC(J2000)	Galactic		Ecliptic	
				$l$	$b$	$\lambda$	$\beta$
MACHO-104-C	104.20251.50	18:03:34.0	–28:00:19	2.797	–2.933	270.790	–4.568
MACHO-96-BLG-5	104.20906.3973	18:05:02.5	–27:42:17	3.219	–3.071	271.119	–4.270
MACHO-96-BLG-12	104.20382.803	18:03:53.2	–27:57:36	2.871	–2.973	270.861	–4.524
MACHO-98-BLG-6	402.48103.1719	17:57:32.8	–28:42:45	1.526	–2.132	268.762	–5.267
MACHO-99-BLG-1	121.22423.1032	18:08:50.0	–30:31:56	1.138	–5.162	271.917	–7.106
MACHO-99-BLG-8	403.47849.756	17:56:25.2	–29:40:31	0.569	–2.401	269.218	–6.237

Table 2. Microlensing Parallax Fit Parameters

Event	$f_{MR}$	$f_{MB}$	$f_{CTIO}$	$f_{MPS}$	$t_0$ (MJD)	$u_{\min}$	$\hat{t}$ (days)	$\tilde{v}$ (km/sec)	$\theta$	$\frac{\chi^2}{(\text{dof})}$	$\Delta\chi^2$
104-C	1.00(1)	0.99(2)			–868.2(6)	0.15(1)	220(2)	77(4)	–1.08(7)	1.47	1051
96-BLG-5	0.12(3)	0.12(3)	0.13(3)		387(1)	0.018(6)	2000(500)	30.9(1.3)	–0.84(6)	1.58	2395
(HST)	0.28(1)	0.30(1)	<b>0.33</b>		391(1)	0.048(6)	970(20)	30.9(1.3)	–0.87(7)	1.59	2371
	0.31(1)	0.33(1)	0.37		392(1)	0.054(7)	900(20)	31.0(1.3)	–0.88(8)	1.59	2363
96-BLG-12	0.87(2)	0.89(3)	0.90(2)		366.9(3)	–0.11(2)	294(5)	47.5(1.3)	–1.23(9)	2.11	5914
98-BLG-6	0.65(14)	0.60(13)	0.68(15)	0.66(13)	1011(3)	0.16(4)	490(50)	79(5)	–1.7(2)	1.20	802
99-BLG-1	0.96(9)	0.98(10)	1.0(1)	0.97(7)	2712(1)	23(2)	219(9)	42.9(9)	–1.85(2)	1.54	1706
99-BLG-8	0.75(12)	0.73(12)	0.76(12)	0.79(13)	1355.6(4)	0.17(1)	240(20)	62(5)	–1.53(3)	2.34	2280

Note. — MJD = JD – 250000 days.

Table 3. Microlensing Parallax Likelihood Mass Estimates

Event	location	$f_{MR}$	$\hat{t}$ (days)	$\hat{v}$ (km/sec)	Confidence Levels $P(M/M_{\odot} < N)$				
					$P = 5\%$	$P = 16\%$	$P = 50\%$	$P = 84\%$	$P = 95\%$
104-C	bulge	1.00(1)	220(2)	77(4)	<b>0.35</b>	<b>0.62</b>	<b>1.15</b>	<b>2.2</b>	<b>3.94</b>
96-BLG-5	bulge	0.12(3)	2000(500)	30.9(1.3)	7.2	12.8	27	69	160
	bulge	0.28(1)	970(20)	30.9(1.3)	<b>1.64</b>	<b>2.93</b>	<b>6.3</b>	<b>15.8</b>	<b>37</b>
	bulge	0.31(1)	900(20)	31.0(1.3)	1.41	2.53	5.4	13.6	31
96-BLG-12	bulge	0.87(2)	294(5)	47.5(1.4)	<b>0.33</b>	<b>0.62</b>	<b>1.29</b>	<b>3.1</b>	<b>6.7</b>
98-BLG-6	bulge	0.65(14)	490(50)	79(6)	<b>0.94</b>	<b>2.6</b>	<b>5.7</b>	<b>12.5</b>	<b>24</b>
	SGR	0.65(14)	490(50)	79(6)	1.23	1.61	2.52	4.2	6.7
	bulge	0.96(9)	219(9)	42.9(9)	<b>0.14</b>	<b>0.29</b>	<b>0.68</b>	<b>1.86</b>	<b>4.6</b>
99-BLG-1	SGR	0.96(9)	219(9)	42.9(9)	0.10	0.16	0.31	0.70	1.51
	bulge	0.75(12)	240(20)	62(5)	<b>0.27</b>	<b>0.56</b>	<b>1.19</b>	<b>2.78</b>	<b>6.0</b>

Note. — Bold-faced type indicates the parameters that are considered to be most likely. Event 96-BLG-5 has parameters for three different fits listed. The first fit is the fit with no constraint on the source brightness, while the second and third fits have the lensed flux fixed to a value based upon our HST observations. The fit labeled HST is the best fit, while the third fit is provided to indicate the effect of the source flux uncertainty on the mass limits. For events 98-BLG-6 and 99-BLG-1, mass estimates based upon bulge and SGR sources are presented. In all cases, it is most likely that the source star is in the bulge.

Table 4. Mass & Magnitude Estimates for the MACHO Microlensing Parallax Events

Event	$M/M_{\odot}$	$M_{\text{MS}}/M_{\odot}$	$D_{\ell-\text{MS}}$	sep-MS	$V_s$	$\Delta I_{\ell s}$	$\Delta V_{\ell s}$	$\Delta B_{\ell s}$	$\Delta U_{\ell s}$
104-C	$1.1^{+1.1}_{-0.5}$	0.74	2.7 kpc	40 mas	17.3	3.5	3.5	3.5	3.2
96-BLG-5	$6^{+10}_{-3}$	-	-	-	-	-	-	-	-
96-BLG-12	$1.3^{+1.8}_{-0.7}$	0.75	2.0 kpc	28 mas	18.0	2.1	2.2	2.2	2.3
98-BLG-6	$2.5^{+1.7}_{-0.9}$	0.88	5.7 kpc	5 mas	20.1	2.2	1.9	1.6	1.1
99-BLG-1	$0.7^{+1.2}_{-0.4}$	0.40	1.7 kpc	17 mas	18.9	1.8	3.2	3.6	3.9
99-BLG-8	$1.2^{+1.6}_{-0.6}$	1.2	1.6 kpc	25 mas	16.3	1.3	0.7	-0.3	-1.1

Note. — These are the parameters of the “most likely” main sequence star lenses for our best microlensing parallax events. For MACHO-96-BLG-5, a main sequence lens is ruled out.